

# Experiments on free-surface turbulence

RALPH SAVELSBERG<sup>†</sup> AND WILLEM VAN DE WATER<sup>‡</sup>

Physics Department, Eindhoven University of Technology, P.O. Box 513,  
5600 MB Eindhoven, The Netherlands

(Received 5 February 2008 and in revised form 23 September 2008)

We study the free surface of a turbulent flow, in particular the relation between the statistical properties of the wrinkled surface and those of the velocity field beneath it. Channel flow turbulence is generated using an active grid. Through a judicious choice of the stirring protocol the anisotropy of the subsurface turbulence can be controlled. The largest Taylor Reynolds number obtained is  $Re_\lambda = 258$ . We characterize the homogeneity and isotropy of the flow and discuss Taylor's frozen turbulence hypothesis, which applies to the subsurface turbulence but not to the surface. The surface gradient field is measured using a novel laser-scanning device. Simultaneously, the velocity field in planes just below the surface is measured using particle image velocimetry (PIV). Several intuitively appealing relations between the surface gradient field and functionals of the subsurface velocity field are tested. For an irregular flow shed off a vertical cylinder, we find that surface indentations are strongly correlated with both vortical and strain events in the velocity field. For fully developed turbulence this correlation is dramatically reduced. This is because the large eddies of the subsurface turbulent flow excite random capillary-gravity waves that travel in all directions across the surface. Therefore, the turbulent surface has dynamics of its own. Nonetheless, it does inherit both the integral scale, which determines the predominant wavelength of the capillary-gravity surface waves, and the (an)isotropy from the subsurface turbulence. The kinematical aspects of the surface-turbulence connection are illustrated by a simple model in which the surface is described in terms of waves originating from Gaussian wave sources that are randomly sprinkled on the moving surface.

---

## 1. Introduction

Turbulent flows in seas and oceans, as well as flows in rivers and channels, are bound by their free surface. Turbulence wrinkles the surface which, in turn, reacts to the subsurface flow. Surface turbulence is important, as the small-scale roughness of the ocean's surface determines the exchange of heat and mass between the atmosphere and the ocean. These transport processes are crucial for the global distribution of momentum, heat and chemical species.

In this paper we will study the wrinkling of the surface in still air. The shape of the surface depends on a delicate balance between vertical acceleration and pressure in the flow below the surface on one hand and gravity and interfacial tension on the other hand. Which force dominates this balance depends on the scale of the

<sup>†</sup> Present address: School of Engineering Sciences, University of Southampton, Highfield, Southampton, SO17 1BJ, UK.

<sup>‡</sup> Email address for correspondence: w.v.d.water@tue.nl

deformation. Generally, for large-scale surface deformations, gravity balances vertical accelerations in the fluid, whereas for smaller scales surface tension plays a more important role. The relative importance of each of these forces can be expressed in terms of two non-dimensional numbers. The Froude number for turbulence with a typical length scale  $L$  and velocity scale  $u$  is

$$Fr = u^2/2gL,$$

where  $g$  is the gravitational acceleration. ( $Fr$  is the ratio of kinetic and potential energy and customarily is  $Fr = u/(gL)^{1/2}$ ). This number is a measure of the potential energy associated with gravity relative to the kinetic energy in the flow. The Weber number, which is the ratio of the flow kinetic energy over the energy due to surface tension, is

$$We = u^2L\rho/2\sigma,$$

where  $\sigma$  is the surface tension coefficient. However, since turbulence does not have a single length scale or time scale, one can expect to see many different features occurring side by side. Brocchini & Peregrine (2001a) classified different types of structures and the behaviour that can occur at a free surface above turbulent flow. The most obvious free-surface deformations are capillary-gravity waves. These travel across the surface and are identifiable by their dispersion relation. Other structures, more closely linked to events in the turbulence, are scars – sharp lines on the surface, most often associated with upwelling or downwelling of fluid. Additionally, low pressure in the core of subsurface eddies can lead to dimples in the surface. This brings us to the central questions in this paper: What does the shape of the free surface reveal about the statistics of the subsurface turbulence? More specifically, if we have clear Kolmogorov scaling of the subsurface turbulence fluctuations, will this scaling also be visible in the surface shape above it? Does the (an)isotropy of the subsurface turbulence determine the (an)isotropy of the surface shape? What part of the turbulence, if any, is directly visible in the surface shape? The answers to these questions are of prime importance for interpreting geophysical observations of the surface shape, obtained by novel remote-sensing techniques (Forbes *et al.* 1993; Stammer 1997).

In a geophysical setting, the large waves one sees at the water surface are driven by the wind above it rather than by the subsurface turbulence. Phillips (1957) proposed resonant initiation of these waves by pressure fluctuations moving with the turbulent wind. Since the phase velocity of free-surface waves on water has the minimum of approximately  $0.23 \text{ m s}^{-1}$ , this resonance mechanism can only work if the turbulent velocity fluctuations are larger than  $0.23 \text{ m s}^{-1}$ . Obviously, this mechanism can also apply to waves generated by turbulence below the surface.

Waves generated by wind have been extensively studied, both in experiments (see, for instance, Zhang 1995) and in simulations (Borue, Orszag & Staroslesky 1995). The latter paper also briefly describes surface waves excited by subsurface turbulence, emerging from the bottom boundary layer in a channel flow in the absence of wind. The resulting surface ripples follow the theoretical dispersion relation for linear gravity-capillary waves reasonably well, except for small wavenumbers. More recently, Teixeira & Belcher (2006) used rapid-distortion theory to calculate both resonant and non-resonant wave growth due to turbulence in the wind above the surface, as well as due to a turbulent subsurface shear flow. They find that subsurface turbulence produces steeper surface waves than (resonant) turbulent

wind fluctuations; so in the initial stages of wave growth, subsurface turbulence is more important than previously thought.

Most studies of the interactions between turbulence and a free surface specifically look at how the presence of a free surface affects the turbulence, rather than at how the turbulence affects the surface. The surface is usually represented by a flat non-deformable stress-free wall, which corresponds to a free surface with very small Froude and Weber numbers. In a study of how turbulence statistics change when an initially homogeneous turbulent flow is convected past a wall moving with the mean flow velocity, Hunt & Graham (1978) introduced the concept of a source layer. In this layer, adjacent to the wall with a depth approximately equal to the integral length of the turbulence, vertical fluctuations are reduced from their values in the bulk to zero at the wall by a source-like velocity distribution. Horizontal fluctuations are adjusted to the boundary condition at the wall in a much thinner viscous layer. Using rapid distortion theory, Hunt & Graham (1978) showed that inside the source layer, while the vertical velocity fluctuations decrease, tangential fluctuations as well as tangential integral scales increase. This agreed with experiments in a windtunnel with a moving wall (Thomas & Hancock 1977). Obviously, turbulence below a (flat) free surface is not the same as turbulence moving past a wall moving at the same velocity, but the overall picture remains the same (Hunt 1984; Teixeira & Belcher 2000; Magnaudet 2003). This has been observed in direct numerical simulations (DNS) of turbulence beneath a free surface. Handler *et al.* (1993), Pan & Banerjee (1995), Nagaosa (1999) and Nagaosa & Handler (2003) simulated a channel flow in which the turbulence originates in the bottom boundary layer. This was also studied by means of large eddy simulation by Calmet & Magnaudet (2003). Perot & Moin (1995) and Walker, Leighton & Garza-Rios (1996) used DNS in an alternative configuration, in which no-slip walls were numerically inserted in initially homogeneous turbulence. The discussion of the turbulence–flow interactions of Brocchini & Peregrine (2001*a*) was fundamental to providing the boundary conditions for splashing surfaces proposed in Brocchini & Peregrine (2001*b*) and complete the analysis of Hong & Walker (2000).

Turbulence under a nearly flat stress-free surface was also studied in experiments; for instance turbulence generated with a vertically oscillating grid (Brumley & Jirka 1987), decaying turbulence behind a towed grid (Loewen, Ahlborn & Filuk 1986) and turbulence generated in the bottom boundary layer in channel flow (Rashidi & Banerjee 1988; Kumar, Gupta & Banerjee 1998).

In order to study how vortical structures affect the shape of the surface, vortex rings are most commonly used, both in experiments (Bernal & Kwon 1989; Song, Bernal & Tryggvason 1992; Gharib & Weigand 1996; Weigand 1996) and numerical simulations (Zhang, Shen & Yue 1999). As a vortex ring approaches a free surface, it tends to break up into smaller vortex tubes that end at the surface (vortex connection). Weigand (1996) combined shadowgraphy and particle image velocimetry (PIV) to show that the locations of the maxima of the vertical component of vorticity, associated with vortex tubes, coincide with the positions at which the surface elevation is the lowest. Song *et al.* (1992), also using shadowgraphy to visualize the free surface shape, report that the process of vortex connection is accompanied by the generation of short waves. However, shadowgraphy only provides a qualitative image of the surface, and obviously, a single structure is not representative of turbulence.

Quantitative measurements allow an assessment of the relative importance of the different types of subsurface structures in determining the shape of the surface. Such experiments were done by Dabiri (2003), combining through the use of PIV a measurement of the velocity field in a plane below the surface, with a measurement

of the surface shape using a two-dimensional free-surface gradient detector (Zhang & Cox 1994).

In another experiment on a shallow turbulent flow running down inclined planes, Smolentsev & Miraghaie (2005) covered a large range of Froude and Weber numbers. Contrary to our work, the surface structure was found to travel with the mean velocity, and no direct evidence for capillary-gravity waves was found. Wave-turbulence interaction in the  $x$ - $z$  plane was studied in a thin (2 cm) liquid plane jet by Li *et al.* (2005). Of the two turbulent velocity components  $u$  and  $w$ , the vertical one showed the strongest correlation with the surface elevation.

Quantitative information on how developed turbulence affects the surface shape so far was only obtained in direct numerical simulations. Tsai (1998) calculated a correlation  $\approx 0.5$  between the surface elevation and the absolute value of the surface-normal vorticity, while the correlation with the parallel vorticity just below the surface was larger ( $\approx 0.7$ ). DNS of turbulent shear flow in a channel with a free surface were also performed by Shen *et al.* (1999) who compared a deformable surface (with linearized boundary conditions) to a flat, non-deformable surface and concluded that in the former case, pressure variations due to upwellings and downdraughts were less pronounced than in the latter, since surface ripples tend to smooth local pressure fluctuations.

In this paper we will quantify the relation between the subsurface turbulence and the surface fluctuations in a well-defined turbulent flow. In our experiments moderately strong turbulence is generated in a water channel, by means of an active grid. The key motivation for choosing this kind of turbulence is that its properties such as homogeneity and isotropy are very well established. However, the turbulence is relatively weak in terms of its surface deformations. With a typical turbulence length scale  $L = 0.1$  m and turbulent velocity  $u = 2.3 \times 10^{-2}$  m s $^{-1}$ , the Froude number is  $Fr = 3 \times 10^{-4}$ , while the Weber number is  $We = 0.4$ , which implies that the surface wrinkles are shallow and rounded (Brocchini & Peregrine 2001a). In our experiments we have access to the two-dimensional subsurface velocity field  $\mathbf{u}(\mathbf{x}, t)$  in planes just below the surface and to the surface gradient field  $\nabla h(\mathbf{x}, t)$  measured along a line. Through long-time averages, various correlations between these quantities can be measured.

### 1.1. Relating the surface shape to the subsurface turbulence

Let us briefly summarize several intuitively appealing relations between two-dimensional slices of the subsurface velocity field in planes parallel to the surface  $\mathbf{u}(\mathbf{x}, t)$  and the surface  $h(\mathbf{x}, t)$  or its gradient field  $\nabla h(\mathbf{x}, t)$ . The simplest relation that can be tried in our experiments is between the magnitude of the vertical component of the vorticity  $|\omega_z|$  and the surface height. In principle  $h$  can be obtained from the measured  $\nabla h$  by integration, but we shall comment on this procedure in §3.

In some special cases the surface elevation associated with a particular vorticity distribution can actually be calculated. For instance for a two-dimensional smoothed Rankine vortex, with radius  $a$ , strength  $\Omega$  and vorticity  $\omega_z(r) = 2\Omega/(1+r^2/a^2)$ , in the absence of surface tension the surface is dimpled as  $h(r) = -(2\Omega^2/a^2)/(1+r^2/a^2)$ . As an alternative we can also consider the decaying vortex with vorticity

$$\omega_z(r, t) = \frac{A}{\nu t^2} \left( 1 - \frac{r^2}{4\nu t} \right) \exp\left( \frac{-r^2}{4\nu t} \right) \quad (1.1)$$

(Taylor 1960), where  $A$  is a measure of the strength of the vortex, and  $\nu$  is the kinematic viscosity of the fluid. The associated circulation is proportional to the time derivative of that of a decaying line vortex. Provided that the vertical velocities

associated with its decay are small, the surface shape above this vortex is Gaussian:

$$h(r, t) = \frac{A^2}{4gvt^3} \left( 1 - \exp\left(-\frac{r^2}{2vt}\right) \right). \quad (1.2)$$

The Navier–Stokes equation for inviscid free surface flow is

$$\frac{\partial \mathbf{u}}{\partial t} + (\mathbf{u} \cdot \nabla) \mathbf{u} = -g \nabla h + \frac{\sigma}{\rho} \nabla(\nabla^2 h), \quad (1.3)$$

where  $\sigma$  is the surface tension, which for a clean air–water interface at room temperature is  $\sigma = 0.73 \times 10^{-3} \text{ N m}^{-1}$  and where the expression for the capillary force assumes small surface elevations. In our experiment we measure the right-hand side of (1.3), which we denote as  $g \zeta$ , whilst from the left-hand side we can measure  $(\mathbf{u} \cdot \nabla) \mathbf{u}$  of velocity fields in planes just below the surface, which we denote as  $g \xi$ . In the stationary case (1.3) suggests a strong correlation between  $\zeta = -\nabla h + (\sigma/\rho g) \nabla(\nabla^2 h)$  and  $\xi = (1/g)(\mathbf{u} \cdot \nabla) \mathbf{u}$ . In order to highlight the relation with vorticity, we may separate the dimensionless two-dimensional acceleration field  $\xi$  into strain  $\mathcal{S}$  and rotation  $\mathcal{Q}$  parts,

$$\xi = \frac{1}{g} (\mathbf{u} \cdot \nabla) \mathbf{u} = \xi_s - \xi_\Omega = \mathbf{u} \cdot (\mathcal{S} - \mathcal{Q}/2)/g, \quad (1.4)$$

and compute the correlation of each of the two parts with the surface force field  $\zeta$  separately. If the surface mainly consists of dimples above subsurface vortex cores, we expect that  $\zeta$  would be most strongly correlated with  $\xi_\Omega$ . On the other hand, if the surface crispations consist of upwellings or downwellings above regions of subsurface strain, the strongest correlation would be with  $\xi_s$ .

Our paper is organized as follows: In §2 we will describe the experimental set-up and characterize the turbulence forced by the active grid. A judicious choice of the forcing protocol allows us to tune the anisotropy of the turbulent flow in the bulk of the channel. Since we have a relatively large mean flow, an interesting question is whether Taylor’s frozen turbulence hypothesis applies. The correlation between the surface and the subsurface velocity fields will be discussed in §3. Several possible connections will first be tested for the irregular vortices shed by a surface-piercing cylinder and subsequently be applied to grid-generated turbulence. The statistical properties of the surface will be described in §4. A simple kinematic model which qualitatively explains the measured surface statistical properties will be discussed in §5.

## 2. Experiment

In our experiments we explore the relation between subsurface velocity fluctuations and the surface wrinkles in a well-defined turbulent flow. We shall first describe the turbulent flow and the way it is generated with help of an active grid. Next we will explain how the subsurface turbulent velocity field and the surface gradient field are measured.

The experiments are done in a water channel, illustrated in figure 1, with a width of 0.3 m, a water depth of approximately 0.31 m and a mean stream velocity of 0–0.3  $\text{m s}^{-1}$ , with a measurement section that is approximately 7 m long. Turbulence is generated either with a static grid or with an active grid (illustrated). For measuring the properties of the turbulence, a two-component laser doppler velocimetry (LDV) is used (not illustrated). It enables the measurement of the vertical and streamwise components of the velocity very close (approx. 1 mm) to the surface. The system is

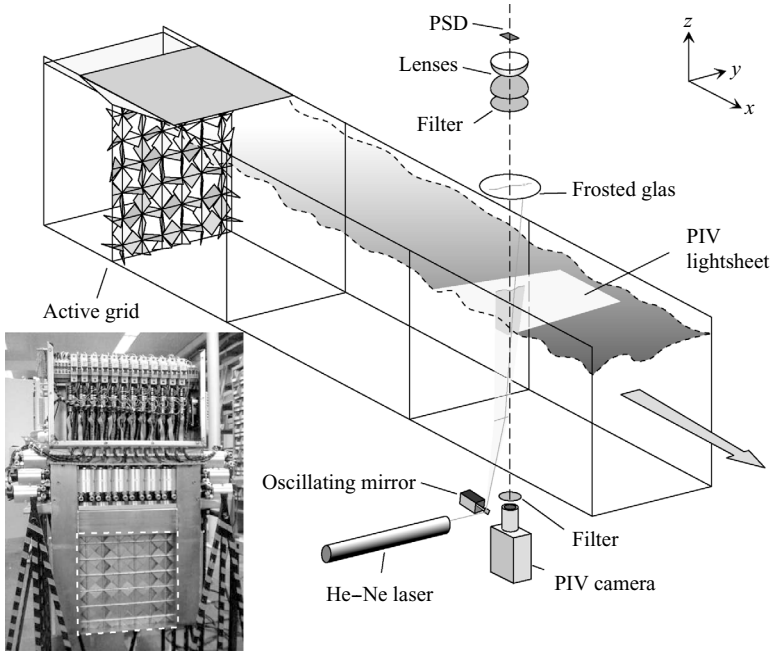


FIGURE 1. Set-up for combined PIV and surface measurements. The inset shows the active grid, with the channel cross-section outlined with the dashed line. In the inset, the vanes of the grid are shown in the parallel configuration; in the experiments we use a staggered arrangement, which improves the isotropy of the generated turbulence. PSD, position sensing device.

mounted on a yoke which allows traversing the location of the measurement volume both in the vertical and spanwise directions. The entire system can also be moved along the channel, to enable measurements at different streamwise locations.

### 2.1. Active grid turbulence

A well-established method to generate approximately homogenous turbulence in a laboratory setting, for instance in a wind tunnel or water channel, is to pass the flow through a grid consisting of vertical and horizontal bars. At a distance of approximately 40 times the mesh size behind the grid and outside of the boundary layers the generated turbulence is a fair approximation of homogeneous and isotropic turbulence, as was shown by, for instance, Comte-Bellot & Corrsin (1966). Within the Kolmogorov framework of turbulence, for a given grid the relation between the Taylor-based Reynolds number  $Re_\lambda$  and the Reynolds number based on the mesh size  $M$  and the main stream velocity  $U$ ,  $Re_M = UM/\nu$ , is given by

$$Re_\lambda = C_f \sqrt{Re_M}, \quad (2.1)$$

with a constant  $C_f$  which depends on the details of the forcing. We define  $Re_\lambda$  in terms of the transverse Taylor microscale  $\lambda_t$  and the turbulence velocity  $u$ :  $Re_\lambda = u\lambda_t/\nu$ . In case of grid turbulence  $C_f$  depends primarily on the type and the solidity of the grid. Poorte (1998) has compared numerous experiments in which turbulence was generated with regular static grids, finding  $C_f$  to be approximately 0.5.

While the turbulence of a static grid is homogeneous and nearly isotropic, it is not strong. A way to increase the turbulence intensity is by using the so-called active grid, which was first used in a wind tunnel by Makita (1991) and later used by Mydlarski & Warhaft (1990). Poorte & Biesheuvel (2002) used a similar grid in a

water tunnel. An active grid consists of an array of axes with metal agitator wings attached to them. Each axis is driven in a random fashion by an electric motor according to a particular forcing protocol. Poorte & Biesheuvel (2002) compared their own experiments with those by Makita (1991) and Mydlarski & Warhaft (1990) who showed that the value of  $C_f$  for active grids is close to 2. Hence, for an active grid,  $Re_\lambda$  is roughly four times larger than for a similarly dimensioned static grid. Poorte (1998) concluded that, in order to generate a fair approximation of isotropic decaying turbulence by use of an active grid, one should use the so-called staggered configuration in which neighbouring agitator wings on each axis of the grid are perpendicular to each other. This was also used in our experiments.

The static grid used in our experiments consists of  $6 \times 6$  mesh openings. The mesh size  $M = 5$  cm, which gives a mesh Reynolds number  $Re_M$  of up to  $1.5 \times 10^4$  and  $Re_\lambda \approx 70$ . The overall solidity is 0.34.

The active grid has mesh size  $M = 5$  cm as well. The grid vanes are mounted in staggered configuration on rods of 5 mm diameter and have a chord of 4.8 cm. A schematic drawing is included in figure 1. The axes of the grid are driven by strong water-cooled motors (Maxon Motors RE 40; 150 W, 48 V) in combination with a 1:4.3 reduction gear (Maxon Motors GP 42) that can switch the rotation speed of an axis from  $-7$  to  $+7$  revolutions per second in only 10 ms. The velocity (but not the position) of each axis is controlled. It is prescribed by a computer program which enables one to impose several forcing protocols. The grid is shown in figure 1. The grid was built as a self-contained unit that could be slotted into the channel from above.

## 2.2. Forcing protocols

The properties of the generated turbulence depend on details of the protocol used to drive the axes. The forcing protocols used here are based on those used by Poorte (1998) and Poorte & Biesheuvel (2002): each axis has a random angular velocity that is changed at random times. According to Poorte two dimensionless numbers are sufficient to describe such forcing protocols for a given grid geometry. The first is the dimensionless angular velocity  $\Omega^*$  based on a comparison of the wing's tip velocity and the mean stream. It is defined as

$$\Omega^* = \frac{\pi \Omega_0 c}{v_0} = \frac{V_{\text{tip}}}{v_0},$$

in which  $c$  is the agitator wing chord;  $v_0$  is the mean stream velocity;  $V_{\text{tip}}$  is the root mean square (r.m.s.) wing tip velocity; and  $\Omega_0$  is the r.m.s. angular velocity. The second dimensionless number is dimensionless time  $T^*$  defined as

$$T^* = \frac{v_0 T_0}{c},$$

where  $T_0$  is the integral time-scale of the forcing protocol, which can be found from the auto-correlation function  $C(\tau)$  of the angular velocity of a given rod. In order to produce homogeneous and isotropic turbulence both dimensionless numbers should be close to unity.

Since in some of the experiments different main stream velocities are used, different protocols matched to the respective velocities are needed. In our experiments these protocols are called (15OPT), (20OPT) and (25OPT) and are aimed at main stream velocities close to 15, 20 and 25  $\text{cm s}^{-1}$ , respectively. They have been designed such that both  $\Omega^*$  and  $T^*$  are indeed close to unity. The turbulence generated with protocol (25OPT) will be compared to turbulence generated with the static grid, which will be

---

name	$U$ ( $\text{m s}^{-1}$ )	$u$ ( $\text{m s}^{-1}$ )	$\frac{u}{w}$	$\epsilon$ ( $\text{m}^2 \text{s}^{-3}$ )	$L_l$ (cm)	$\lambda_t$ (cm)	$Re_\lambda$	$\eta$ (mm)	$(\frac{\partial h}{\partial x})_{\text{r.m.s.}}$	$(\frac{\partial h}{\partial y})_{\text{r.m.s.}}$
15OPT	0.166	$9.70 \times 10^{-3}$	1.05	$8.5 \times 10^{-6}$	6.9	1.30	125	0.59	$3.6 \times 10^{-3}$	$4.1 \times 10^{-3}$
20OPT	0.221	$1.27 \times 10^{-2}$	1.05	$2.4 \times 10^{-5}$	6.3	1.00	128	0.45	$7.7 \times 10^{-3}$	$7.6 \times 10^{-3}$
25OPT	0.271	$1.62 \times 10^{-2}$	1.10	$4.2 \times 10^{-5}$	7.0	0.97	157	0.39	$1.6 \times 10^{-2}$	$1.6 \times 10^{-2}$
25RAN	0.266	$2.29 \times 10^{-2}$	1.15	$6.2 \times 10^{-5}$	8.1	1.10	258	0.36	$2.7 \times 10^{-2}$	$2.6 \times 10^{-2}$
25STAT	0.289	$7.50 \times 10^{-3}$	1.10	$9.4 \times 10^{-6}$	3.5	0.95	71	0.57	$9.6 \times 10^{-3}$	$9.4 \times 10^{-3}$

---

TABLE 1. Overview of turbulence properties measured on the centreline of the channel at 2 m behind the grid and 10 cm below the surface.  $L_l$  is the longitudinal integral scale,  $\lambda_t$  the transverse Taylor microscale and  $\eta$  the Kolmogorov scale. The Taylor-based Reynolds number is  $Re_\lambda = u\lambda_t/\nu$ , with the kinematic viscosity of water  $\nu = 10^{-6} \text{ m}^2 \text{ s}^{-1}$ . The last two columns show r.m.s. values of the surface slope in streamwise ( $x$ ) and spanwise ( $y$ ) directions.

referred to as (25STAT), as well as with another protocol for the active grid (25RAN). In the latter, each axis receives a different random angular velocity that is changed at a fixed frequency. The maximum velocity is  $14 \text{ rev s}^{-1}$ , which is much higher than for any of the others, and the velocity is changed at a fixed frequency of 7 Hz. As we will show later, the turbulence generated by the static grid and the OPT protocol is close to isotropic, while the RAN protocol produces markedly anisotropic turbulence. This will enable us to study the influence of the bulk turbulence anisotropy on the turbulent free surface.

### 2.3. Properties of the turbulence

Most measurements are done at 2 m from the grid (40 times the mesh size), where the turbulence can be expected to be fully developed (Comte-Bellot & Corrsin 1966). The LDV measurements correspond to the most common way of measuring turbulence properties: through a point measurement of one or multiple components of the velocity as a function of time. Correlation functions and spectra can only be measured in time, but by using the Taylor hypothesis, time can be transformed into the streamwise spatial coordinate.

The turbulence properties measured for the different forcing protocols as well as the static grid, denoted with 25STAT, are listed in table 1. It is immediately clear from this table that the streamwise fluctuation velocity  $u$  varies widely with the forcing. The static grid leads to the lowest turbulence intensity, 2.6 %, while depending on the protocol; for the active grid it varies from 5.6 % to 8.8 %. With comparable mean velocity, the Taylor Reynolds number for the near-isotropic turbulence generated by the active grid is  $Re_\lambda = 157$ , while for the static grid it is  $Re_\lambda = 71$ . The spectra for these two cases are shown in figure 2. These and other spectra were used to compute the viscous dissipation  $\epsilon$ , while the (transverse) Taylor length scale  $\lambda_t$  and the longitudinal integral length scale  $L_l$  were calculated from the companion correlation functions. The Taylor microscale can also be determined from the dissipation rate; the result is within 10 % of the value in table 1. The dissipation rate can also be inferred from a measurement of the decay of the turbulent kinetic energy with  $x$ . We found  $u^2 \sim x^{-\kappa}$ , with an exponent  $\kappa$  close to one, but its precise value depends on the mode of operation of the grid. The dissipation rate deduced from the decay of the kinetic energy was within 10 % of that measured from the spectrum. Because the grid protocol has to be changed with a change of the mean velocity, the Reynolds numbers for the active grid do not always show a large increase with increasing mean velocity.



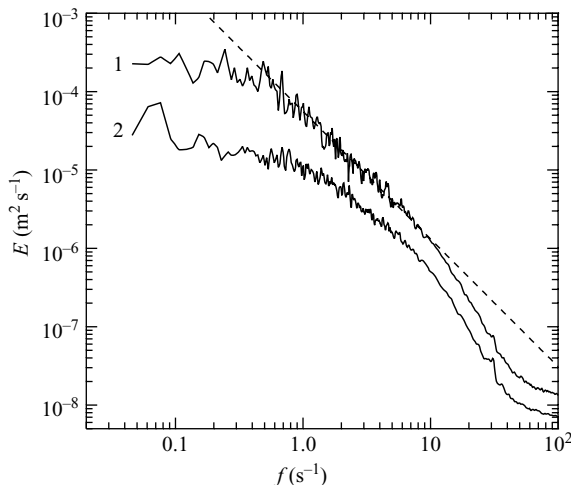


FIGURE 2. Longitudinal energy spectra for the static grid and the active grid with protocol (25OPT), measured 10 cm below the surface and 2 m behind the grid. Full line 1: active grid (25OPT in table 1); full line 2: static grid with protocol 25STAT in table 1; dashed line: fit of  $E(k) = C_K \epsilon^{2/3} k^{-5/3}$ , with  $C_K = 0.55$  (Pearson, Krogstad & van de Water 2002), which was also used to determine  $\epsilon$ .

Figure 3(a) shows profiles of the mean-stream velocity for both the active and static grids, for the same setting of the water channel pump. As can be expected in turbulent channel flow, these profiles show a region near the channel centre in which the mean-stream velocity is practically constant, flanked by the boundary layers from the channel walls. Due to the higher blockage of the active grid, the mean-stream velocity is somewhat lower than in case of the static grid.

The variation of both  $u$  and  $w$  turbulent velocity components across the channel is shown in figure 3(c–f). Close to the surface the vertical turbulent velocity decreases, while the horizontal velocity increases. Consequently, the turbulent ( $u, w$ ) anisotropy sharply increases near the surface. These observations are in full agreement with the existence of a source layer: a layer below the surface, with a thickness of roughly one integral length scale, in which energy is redistributed from vertical to horizontal fluctuations. The bottom boundary layer cannot be seen in these measurements, since it lies outside of the vertical range over which the measurement volume can be traversed.

Overall, these measurements show that at 2 m behind the grid, in a region of approximately 10 cm width near the centre of the channel and up to 6 cm below the surface, the turbulence generated by both the active and static grids is approximately homogeneous in both the spanwise and vertical directions. Due to the presence of the surface and the associated source layer, the turbulence is no longer homogeneous as we move closer to the surface, and it obviously is not homogeneous inside the boundary layers formed on the channel walls. Since the turbulence decays, the turbulence is obviously not homogeneous in the streamwise direction. However, since at 2 m we are relatively far removed from the grid the turbulence decays relatively slowly. Consequently, over a relatively small volume at 2 m from the grid, far below the surface and near the channel centreline, the turbulence can be considered approximately homogeneous.

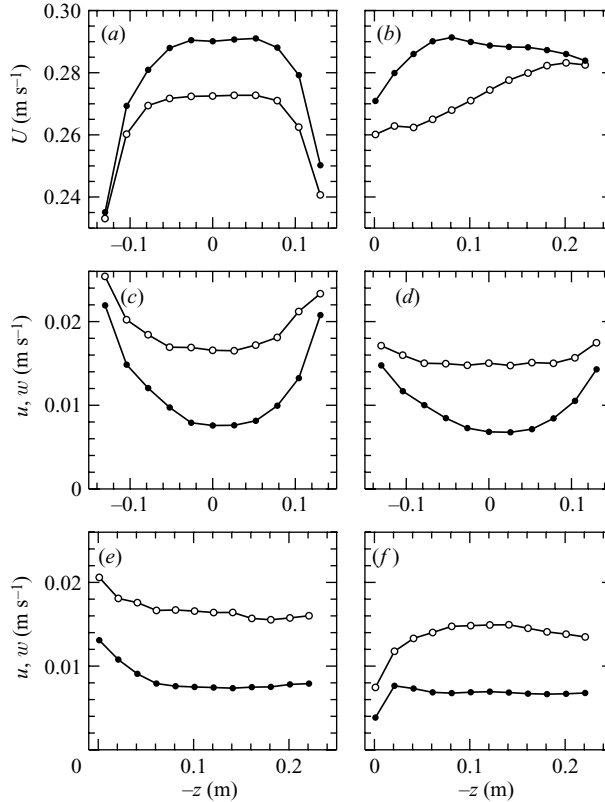


FIGURE 3. Velocity profiles the turbulence in the channel. Open circles: turbulence generated with the active grid (25OPT in table 1); closed dots: static grid (25STAT in table 1). (a) Spanwise profiles of the mean-stream velocity  $U$ . (b) Depth profiles of  $U$ . Spanwise profiles of (c) streamwise turbulent velocity  $u$  and (d) vertical turbulent velocity  $w$  measured at 0.1 m below the surface at 2 m downstream from the grid. Vertical profiles of (e) streamwise turbulent velocity  $u$  and (f) spanwise fluctuation velocity  $w$  measured at the centreline of the channel ( $y=0$ ) at 2 m downstream from the grid.

A point of concern is the direct excitation of the waves by the active grid. These were suppressed by capping the surface directly above the grid (see figure 1). At the measurement location most of these waves will have damped out. Moreover, in §4 it is shown that the wrinkled surface is isotropic. A consequence of this cap is that in figure 3(b) the surface mean velocity is slightly smaller than its bulk value.

#### 2.4. PIV and surface gradient measurements

The  $u, v$  components of the subsurface velocity field in planes below the surface are measured with PIV. A dual pulsed Nd:YAG laser (Spectron Lasers SL454; 200 mJ per pulse, 15 pulse pairs per second) is used as the light source for producing a 1 mm thick horizontal light sheet below the surface. A digital camera (Kodak ES 1.0; 8 bit,  $1018 \times 1008$  pixels) is mounted below the water channel pointing upwards. It images an area of approximately  $5.5 \times 5.5 \text{ cm}^2$  of the light sheet. For both the LDV measurements and the PIV, the flow is seeded with  $100\mu\text{m}$  glass seeding particles (Dantec).

The measured velocity field is a spatial average over the used  $32 \times 32$  pixel interrogation window, which corresponds to an area of  $2 \times 2 \text{ mm}^2$  in the actual

flow. We use a 50 % overlap between adjacent interrogation windows. With these choices we found that the relative amount of spurious velocity vectors lies below 1 %. Additionally, the velocity field is filtered using a Gaussian kernel  $\exp(-r^2/\sigma_G^2)$  with Gaussian width  $\sigma_G = 7$  mm, which corresponds to  $\sigma_G \approx 15 \eta$  at the largest Reynolds number. This filter influences the correlations discussed in §3; they are optimal with the chosen  $\sigma_G$ .

The surface gradient field is measured in space and time by means of a newly developed laser scanning technique. A harmonically swivelling laser beam is focused on the surface, and its angle of refraction is measured using a position sensing device. Details of this device can be found in Savelsberg, Holten & van de Water (2006). Thus, a measurement of both components of the surface gradient field  $\nabla h$  can be obtained along a line. By rotating the entire scanning device, this line can be oriented in either the streamwise or the spanwise direction. The scanning frequency is kept at 2 kHz, so that the lines provide an instantaneous view of the gradient field along the line. The scanning device produces a highly linear view of the gradient field in 152 points on the line. Currently, its spatial resolution is limited by the finite time response (a few  $\mu$ s) of the position-sensitive device. Calibration of the measurement of  $\nabla h$  only needs the length of the average line and the distance of the detector above the surface; all other information can be obtained from the data (Savelsberg *et al.* 2006).

The entire optical system is aligned such that the surface scan line lies close to the centre of the PIV image. This is done with help of a calibration grid that defines both coordinates in the PIV plane and the location of the surface-scanning laser line. Not only should the data be located on the same spatial coordinates, but it should also be obtained at the same time. A given PIV snapshot needs to be matched to the correct part of the surface scan data and vice versa. Synchronization is achieved by means of a purpose-built electronic timing unit. This timing unit also forms the clock of the PIV system: a pair of PIV images is taken once after every 131st scan line. In this way a strict temporal synchronization of both surface and subsurface turbulence measurement systems remains guaranteed.

If the surface is scanned along lines at times  $t_i, i = 1, \dots$ , perpendicular to the mean stream velocity, it is tempting to employ Taylor's frozen turbulence hypothesis and tile these lines to  $(x_i, y)$  surfaces. The reconstruction is done such that  $x_i = U(t_i - t_k)$ , where  $t_k, k = 1, \dots$ , are the subsequent times of the PIV snapshots, and the line samples at  $t_i$  are chosen such that  $-L/2 \leq x_i \leq L/2$ . Therefore, only the central line  $x_i = 0$  of each reconstructed surface coincides exactly with the time at which the corresponding PIV snapshot of the velocity field is taken. We will discuss this procedure and its caveats in depth in §2.7, and again in §4, but end this section with a series of planar snapshots of a turbulent surface in figure 4.

We can clearly distinguish localized surface bumps and dimples, together with line-like scars and ridges. Due to the used-tiling procedure, the observed convection in the  $x$  direction (vertical in the snapshots) is only meaningful if Taylor's frozen turbulence hypothesis applies to the surface. The surface scanning technique is very accurate: the r.m.s. height variation in figure 4 is a mere  $\langle h^2 \rangle^{1/2} = 0.1$  mm. However, a notable advantage is that the scanning probe provides direct access to the surface 'gradient' field.

### 2.5. Isotropy of the subsurface turbulence

For grid-generated turbulence, outside of the boundary layers, isotropy in planes perpendicular to the mean-stream direction is practically assured. However, measurements in other planes often show anisotropy. The simplest measure of isotropy is the ratio of fluctuation velocity components, in case of our LDV measurements,

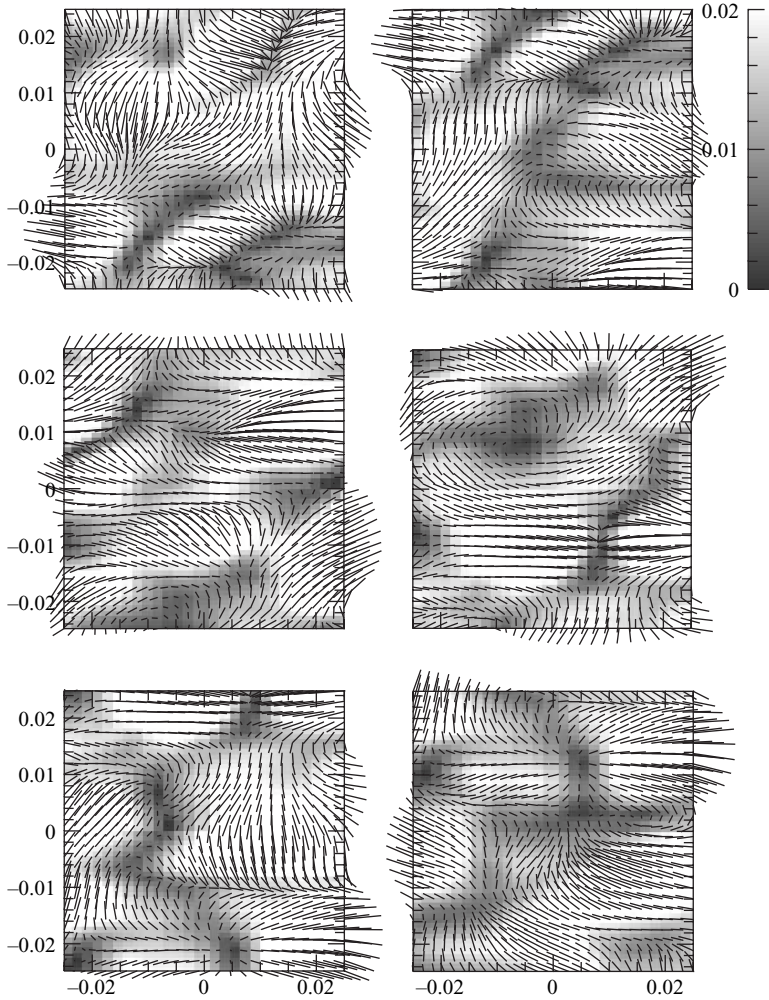


FIGURE 4. Surface gradient field scanned in the spanwise ( $y$ ) direction, with lines tiled into surfaces,  $x = Ut$ , with the mean stream velocity  $U = 0.25 \text{ m s}^{-1}$ . The time separation of the frames is  $0.128 \text{ s}$ , which is twice the temporal separation of the corresponding subsurface PIV images; the time increases from the upper left to the lower right frame.

the ratio of  $u$  over  $w$ . Its value, for the various protocols, is listed in table 1. For static grids a difference between the streamwise and vertical r.m.s. velocities of up to 10% is fairly common (Comte-Bellot & Corrsin 1966), and indeed for our static grid we find a 10% difference. The difference for the active grid ranges from 5% to 15%. Interestingly, in general an increase of turbulence intensity is accompanied by an increase in the difference between  $u$  and  $w$ , which was already noted for the comparison of various static grids by Comte-Bellot & Corrsin (1966).

A comparison of the turbulent velocities only reveals anisotropy existing at large scales. Scale-dependent anisotropy information can be obtained through analysis of correlation functions of the velocity field. These were measured with PIV in horizontal planes 10 cm beneath the surface. The normalized spatial correlation function for a

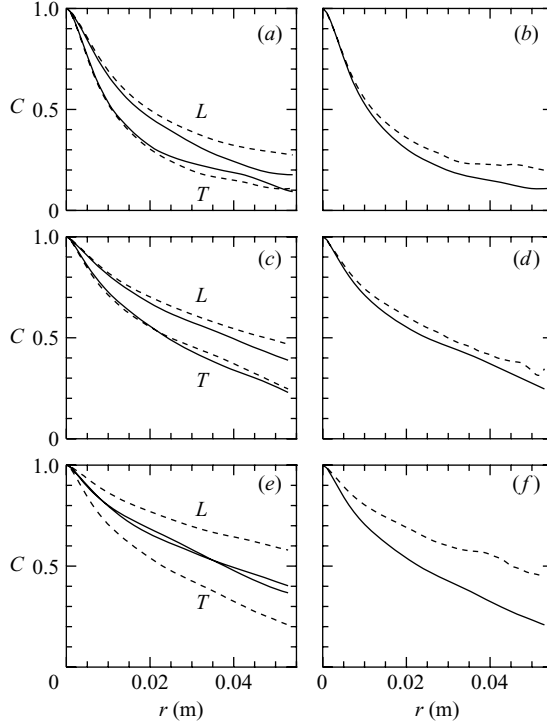


FIGURE 5. Longitudinal  $C_{\beta\beta}(\mathbf{r}\mathbf{e}_\beta)$  ( $L$ ) and transverse  $C_{\alpha\alpha}(\mathbf{r}\mathbf{e}_\beta)$  ( $T$ ) correlation functions of the velocity field measured 10 cm below the free surface. (a) Near-isotropic turbulence stirred by the passive grid (25STAT in table 1); full lines:  $\beta = x$ ; dashed lines  $\beta = y$ . (b) Full line: transverse  $C_{xx}(\mathbf{r}\mathbf{e}_y)$  from (a); dashed line:  $C^T$  computed from the longitudinal  $C_{yy}(\mathbf{r}\mathbf{e}_y)$  from (a) using the isotropy relation (2.3). (c) Near-isotropic turbulence stirred by the active grid (25OPT in table 1); full lines:  $\beta = x$ ; dashed lines  $\beta = y$ . (d) Full line:  $C_{xx}(\mathbf{r}\mathbf{e}_y)$  from (c); dashed line:  $C^T$  computed from  $C_{yy}(\mathbf{r}\mathbf{e}_y)$  from (c), using the isotropy relation (2.3). (e) Anisotropic turbulence (25RAN in table 1); full lines:  $\beta = x$ ; dashed lines  $\beta = y$ . (f) Full line:  $C_{xx}(\mathbf{r}\mathbf{e}_y)$  from (e); dashed line:  $C^T$  computed from  $C_{yy}(\mathbf{r}\mathbf{e}_y)$  from (e) using the isotropy relation (2.3).

homogeneous field is taken as

$$C_{\alpha\alpha}(\mathbf{r}\mathbf{e}_\beta) = \frac{\langle u_\alpha(\mathbf{x} + \mathbf{r}\mathbf{e}_\beta)u_\alpha(\mathbf{x}) \rangle - \langle u_\alpha \rangle^2}{\langle (u_\alpha(\mathbf{x}) - \langle u_\alpha(\mathbf{x}) \rangle)^2 \rangle}, \quad (2.2)$$

where the velocities are all measured at the same time. From the possible combinations of the measured velocity component  $u_\alpha$  and the direction  $\mathbf{e}_\beta$ , the ‘longitudinal’ correlations  $C^L(r)$  are  $C_{xx}(\mathbf{r}\mathbf{e}_x)$  and  $C_{yy}(\mathbf{r}\mathbf{e}_y)$ , while the ‘transverse’ correlations  $C^T(r)$  are  $C_{xx}(\mathbf{r}\mathbf{e}_y)$  and  $C_{yy}(\mathbf{r}\mathbf{e}_x)$ . Isotropy and incompressibility of a three-dimensional velocity field implies that

$$C^T(r) = C^L(r) + \frac{r}{2} \frac{d}{dr} C^L(r). \quad (2.3)$$

By comparing the transverse correlation function that is computed from a measured longitudinal one using (2.3) to an actually measured transverse correlation function, the isotropy of our grid-generated turbulence is tested.

Figure 5 shows results for different types of forcing. Clearly, the turbulence generated with the 25RAN protocol is already anisotropic for small scales, while

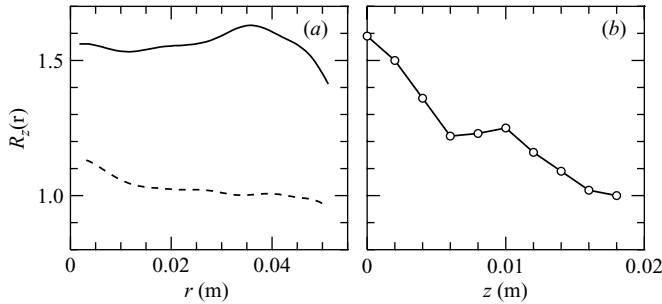


FIGURE 6. The presence of the surface is felt in the anisotropy ratio  $R_z(r)$  (2.4) which is computed from planar cuts of the velocity field at increasing depth  $z$  below the surface. (a)  $R_z(r)$  at  $z=0$  (full line) and  $z=0.018$  m (dashed line). (b) Depth dependence of  $R_z(r)$  at  $r=0.03$  m ( $=73 \eta$ ).

the flow generated by both the OPT and STAT protocols is close to isotropic. We conclude that a judicious choice of the stirring protocol can produce anisotropic turbulence in our experiments. This will be used later on when we shall relate the isotropy of the surface crispations to that of the subsurface turbulence.

### 2.6. Depth dependence of isotropy

In contrast to the three-dimensional velocity field in the bulk, the two-dimensional surface velocity field  $(u_x, u_y)$  is compressible. The interesting consequences for the dispersion of surface contaminants has been explored recently in experiments and numerical simulations by Cressman *et al.* (2004). In their simulations the free surface was assumed flat, while their experiments tried to avoid surface ripples as much as possible. It was found that the normalized planar divergence of the velocity field

$$C = \langle (\partial_x u_x + \partial_y u_y)^2 \rangle / (\langle (\partial_x u_x)^2 \rangle + \langle (\partial_x u_y)^2 \rangle + \langle (\partial_y u_x)^2 \rangle + \langle (\partial_y u_y)^2 \rangle),$$

whose isotropic value is  $1/6$ , tends to  $C \approx 0.5$  at the surface. However, it is unclear why this would be so. In our experiments we measure the  $u, v$  components of the velocity field in planes at various depths below the (average) free surface. Because the size of the interrogation window in our PIV procedure is several times the Kolmogorov length scale  $\eta$ , we cannot measure the divergence of the velocity field. However, an interesting ‘inertial-range’ quantity is the ratio

$$R_z(r) = \left( S_2^L(r) + \frac{r}{2} \frac{dS_2^L}{dr} \right) / S_2^T(r), \quad (2.4)$$

where  $S_2^L$  is the second-order structure function of the velocity. This quantity is 1 only if there is isotropy, not only in the  $(x, y)$  plane but also in the vertical ( $z$ ) direction, although the corresponding  $w$  velocity component does not play a role in (2.4).

In figure 6(a) we plot the ratio  $R_z(r)$  at different depths, and in figure 6(b) we show the depth dependence of  $R_z(r)$  at  $r/\eta = 73$ , which is within the inertial range. At the surface  $R_z(r)$  tends to 1.5 and shows little variation with  $r$ . It is remarkable that the proximity of the surface is felt by an isotropy function of the planar velocity field. The decay depth of  $R_z(r)$  can be compared to the thickness of the anisotropy layer in figure 3(b, e).

### 2.7. The validity of Taylor’s hypothesis

In our experiment the information about the surface gradient field comes in the form of lines, which are measured virtually instantaneously. Assuming that the entire

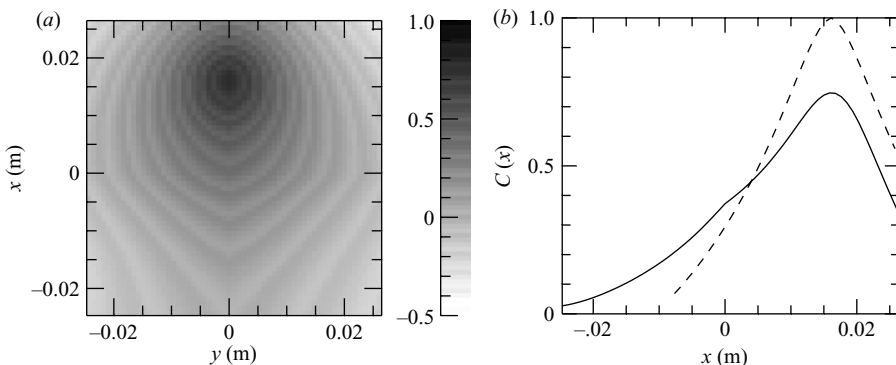


FIGURE 7. (a) Space–time correlation function  $C(\mathbf{r}, \tau)$  of the subsurface velocity field (at the depth  $z=0$ ) and fixed  $\tau = \tau_0 = 0.0642$  s. (b) Full line: correlation function of the subsurface velocity field  $C(x, y=0; \tau_0)$ ; dashed line  $C(x + U\tau_0, y=0; 0)$ .

surface is frozen and advected with the mean velocity, we tile these lines into planar snapshots in figure 4. This assumption is equivalent to Taylor’s frozen turbulence hypothesis.

Let us illustrate Taylor’s hypothesis for the subsurface ‘velocity field’ by correlating at a time interval two subsequent PIV snapshots of  $\mathbf{u}(\mathbf{x}, t)$ , taken of  $\tau_0 = 0.0642$  s apart. In figure 7 we show the normalized spatial correlation function of the velocity field,

$$C(\mathbf{r}, \tau) = \frac{\langle \mathbf{u}(\mathbf{x} + \mathbf{r}, t + \tau) \cdot \mathbf{u}(\mathbf{x}, t) \rangle}{\langle u^2(\mathbf{x} + \mathbf{r}, t + \tau) \rangle^{1/2} \langle u^2(\mathbf{x}, t) \rangle^{1/2}},$$

and compare it to the instantaneous spatial correlation function  $C(\mathbf{r}, \tau = 0)$ . Taylor’s hypothesis implies that  $C(\mathbf{r} + U\tau\mathbf{e}_x, 0) = C(\mathbf{r}, \tau)$ . Although  $C(\mathbf{r}, \tau_0)$  has its maximum at  $x = U\tau_0$ , it is smaller than 1. This discrepancy is due to the fluctuations of the advection velocity and the acceleration terms on the right-hand side of the Navier–Stokes equation (Gledzer 1997) and is mainly caused by the short time scales.

In figure 4, where we display surface ‘snapshots’ of the gradient field, we employ Taylor’s hypothesis, assuming that the frozen surface is advected by the mean velocity  $U$ . As was argued in Savelsberg *et al.* (2006) and as will be again demonstrated in §4, this is not correct. It will appear that the surface texture is only advected ‘in the mean’ with  $U$ . Structures travel on the surface in all directions with the phase velocity of capillary–gravity waves. Therefore, a more cautious interpretation of figure 4 is as space–time plots. However, we believe that the identification of surface features in figure 4 such as scars and ridges still applies.

### 3. Correlation of the surface gradient field with the subsurface velocity field

In figure 4 we have shown surfaces reconstructed from line scans of the surface gradient field using Taylor’s frozen turbulence hypothesis. In this way the reconstructed planar field  $\nabla h(\mathbf{x}, t)$  coincides in time and space with the snapshots of the subsurface velocity field on  $(x, y) = [-L/2, L/2; -L/2, L/2]$ . This reconstruction enables us to compute the planar  $(x, y)$  correlation between these two fields.

However, in §2.7, we found that Taylor’s hypothesis works poorly for the moving surface. Strictly speaking, therefore, we may only correlate the velocity field at times  $t_0$  on the line  $[x=0; y \in -L/2, L/2]$  with the line scan of  $\nabla h(\mathbf{x}, t)$  that was taken

exactly simultaneously with the PIV image. Since we can now only use the velocity field on a line for computing the correlation function, its statistical accuracy will be degraded.

In fact, the computation of planar correlation functions by using reconstructed surface measurements amounts to a filtering action. That is we emphasize those surface structures that travel with the mean flow velocity  $U$  which was used in the Taylor reconstruction of the surface. Conversely, we may view the reconstruction procedure in the time domain and translate the  $x$ -coordinate of the measured velocity field into time, using Taylor's hypothesis for the velocity field. However, using Taylor's hypothesis in this manner also amounts to filtering structures in the correlation function that travel with the mean velocity. That Taylor's hypothesis works well for the velocity field and poorly for the surface gradient field is not relevant in this respect: in both views we filter structures in the planar correlation functions. To study the effect of filtering, we will compute correlations on both a line  $y$  and the reconstructed  $x, y$  plane.

As explained in § 1.1, the simplest correlation would be between the surface elevation  $h$  and the magnitude  $|\omega_z|$  of the vertical component of the vorticity. A problem is that in our experiment we measure the surface gradient field  $\nabla h$  and not the elevation  $h$ . Therefore,  $h$  must be obtained from  $\nabla h$  by integration. For this integration, a reference point  $\mathbf{x}_0$  at which the surface height is zero must be chosen. In our experiments we compute  $h$  from  $\nabla h$  by averaging over all possible reference points,

$$h(\mathbf{x}, t) = \left\langle \int_{\mathbf{x}_0}^{\mathbf{x}} \nabla h(\mathbf{x}', t) d\mathbf{x}' \right\rangle,$$

and set the spatial average of the instantaneous height to zero,  $\langle h(\mathbf{x}, t) \rangle_{\mathbf{x}} = 0$ .

In our experiment we are interested in 'fluctuations' of the elevation. Because the size  $L$  of the surface is finite and because the correlation length is comparable to  $L$ , we will miss the fluctuations on scales comparable to  $L$ . The consequence is that the elevation fluctuations of such a surface obtained by integration of its gradient depend on the position  $\mathbf{x}$ . For a one-dimensional surface  $h(x, t)$  that is obtained by integration of  $h_x(x, t)$  such that  $\langle h(x, t) \rangle_t = 0$ , it can be readily derived that

$$\langle h^2(x, t) \rangle_t = \langle \tilde{h}^2 \rangle - \frac{2}{L} \int_{-x}^{L-x} C_{\tilde{h}, \tilde{h}}(x') dx' + \frac{2}{L^2} \int_0^L (L-x') C_{\tilde{h}, \tilde{h}}(x') dx',$$

where  $\langle \tilde{h}^2 \rangle$  is the variance of the true surface height  $\tilde{h}$  and  $C_{\tilde{h}, \tilde{h}} = \langle \tilde{h}(x'+x, t) \tilde{h}(x, t) \rangle_{x', t}$  is its correlation function. As expected, if the surface is delta-correlated or if the surface size  $L$  is infinitely large, the surface elevation variance is independent of  $x$  and equal to the true surface variance. The consequence of the ambiguity of the surface reference height is that all measured correlations involving the surface elevation show a spurious  $x$  dependence.

The correlation between the surface elevation and the absolute value of the vorticity component,  $|\omega_z|$ , is defined as

$$C_{|\omega_z|, h}(\mathbf{r}) = \frac{\langle |\omega_z(\mathbf{r}' + \mathbf{r}, t)| h(\mathbf{r}, t) \rangle_{\mathbf{r}', t}}{\langle \omega_z^2(\mathbf{r}, t) \rangle^{1/2} \langle h^2(\mathbf{r}, t) \rangle^{1/2}},$$

where we make sure that the fields  $|\omega_z|$  and  $h$  have zero mean by appropriate shifts, for example replacing  $|\omega_z|$  by  $|\omega_z| - \langle |\omega_z| \rangle_t$ . The correlation function on lines,  $C_{|\omega_z|, h}^l(y)$ , which does not use Taylor's hypothesis, is defined analogously. For vector fields  $\boldsymbol{\alpha}$ ,  $\boldsymbol{\beta}$



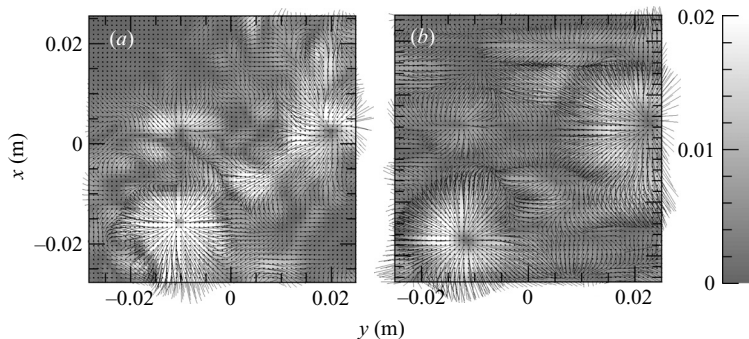


FIGURE 8. Relation between the velocity field and the free surface deformations of the turbulent flow behind a cylinder. The mean flow velocity is  $0.16 \text{ m s}^{-1}$ ; the cylinder diameter is  $1.2 \text{ cm}$  ( $Re = 1.9 \times 10^3$ ). (a) The normalized convective acceleration  $\xi = -(\mathbf{u} \cdot \nabla)\mathbf{u}/g$  computed from velocity fluctuations  $\mathbf{u}$  that were measured in a plane  $1 \text{ mm}$  below the surface. (b) measured surface gradient field  $\nabla h$ . Two large vortices can be seen, where the fields  $\xi$  and  $\nabla h$  are strikingly similar; elsewhere, they are different. Clearly, the field  $\xi$  picks out the large-scale depressions of the surface.

the equal-time correlation function is similarly defined:

$$C_{\alpha,\beta}(\mathbf{r}) = \frac{\langle \alpha(\mathbf{r} + \mathbf{r}', t) \cdot \beta(\mathbf{r}', t) \rangle}{\langle \alpha \cdot \alpha \rangle^{1/2} \langle \beta \cdot \beta \rangle^{1/2}},$$

where it has again been made sure that the fields  $\alpha$ ,  $\beta$  have zero mean.

For measurement of the correlation function, a few technicalities should be considered. As the surface gradient field  $\nabla h$  is traced by the harmonically scanning laser beam, it is resampled such that both the (resampled) velocity field  $\mathbf{u}(\mathbf{x}, t)$  and the resampled gradient field occur on the same discrete grid  $(x_i, y_i)$ ,  $i = 1, \dots$ , and correlations between the two fields can be computed in practice. We estimate that the spatial resolution of the measured  $\nabla h$  field is approximately  $3\eta$  at the highest Reynolds number. The derivative fields  $\nabla^2 h$  and  $\nabla(\nabla^2 h)$  are computed by fitting local quadratic surfaces with size  $5\eta \times 5\eta$  to the measured  $\nabla h(\mathbf{x}, t)$ . At each Reynolds number and depth below the surface correlations are averaged over  $10^3$  measured frames. As figure 7(b) illustrates, these frames are nearly independent.

### 3.1. Vortex shedding

We shall first illustrate our methods by a measurement of the irregular shedding of vortices off a vertical surface-piercing cylinder. For these experiments the grid was removed from the water channel, and a cylinder with a diameter of  $1.2 \text{ cm}$  was placed in the measurement section of channel instead; based on the cylinder diameter, the Reynolds number was  $Re_D = 1.9 \times 10^3$ . The distance between the measurement location and the cylinder was  $40 \text{ cm}$ , which is 33 times the cylinder diameter. At this Reynolds number, the wake is turbulent but with vortices still clearly visible.

Figure 8 compares a snapshot of the field  $\xi(\mathbf{x}) = (1/g)(\mathbf{u} \cdot \nabla)\mathbf{u}$  with  $\nabla h(\mathbf{x})$ . The fields are drawn on the same scale, and as was anticipated in §1.1, they bear a striking resemblance to each other. This resemblance is quantified by the correlation functions  $C_{\xi,\nabla h}$  and  $C_{|\omega_z|,h}$  shown in figure 9. While figure 9(a,b) show the planar correlation functions assuming Taylor's hypothesis for the surface gradient field, the corresponding line correlations are shown in figure 9(c). We also show the strain correlation  $C_{\xi_s,\nabla h}$  and its rotation companion  $C_{\xi_\Omega,\nabla h}$ .

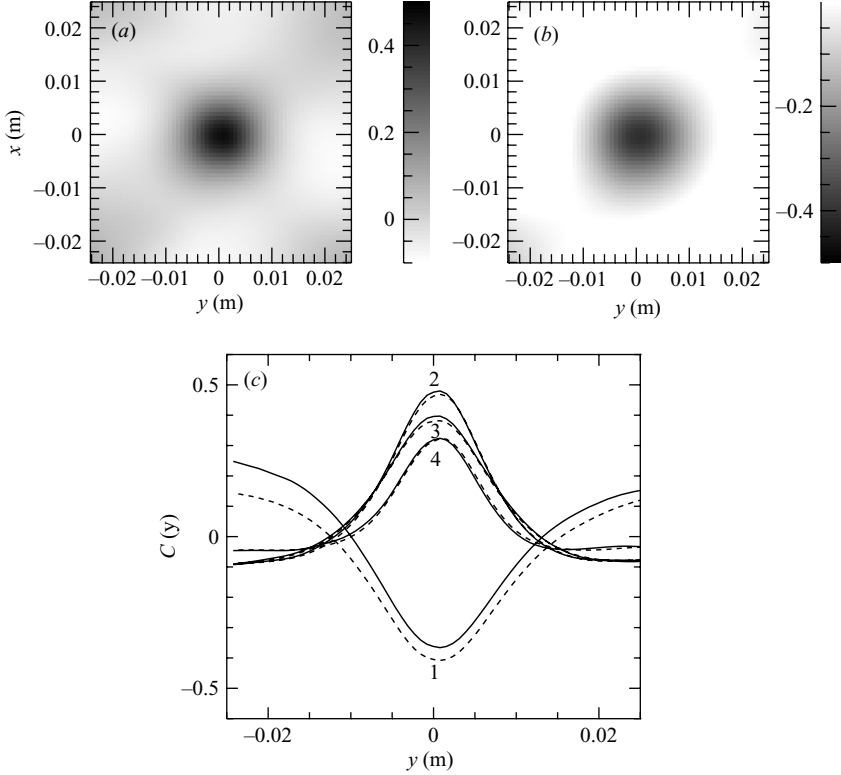


FIGURE 9. Correlations in vortex shedding. Planar correlation functions (a)  $C_{\xi, \nabla h}(\mathbf{r})$  and (b)  $C_{|\omega_z|, h}$ . The vertical ( $x$ ) coordinate of the surface gradient field was reconstructed using Taylor's hypothesis. (c) Full lines: line correlation functions and  $C_{|\omega_z|, h}^l(y)$  (1),  $C_{\xi, \nabla h}^l(y)$  (2),  $C_{\xi_S, \nabla h}^l(y)$  (3) and  $C_{\xi_\omega, \nabla h}^l(y)$  (4). The dashed lines are the corresponding planar correlation functions at  $x=0$ . The line correlations do not use Taylor's hypothesis.

The line correlations  $C^l(y)$  shown in figure 9(c) are compared with a line at  $x=0$  from the corresponding planar correlation functions. The latter filter structures which travel with the mean velocity but do not significantly differ from  $C^l(y)$ . Therefore, all structures of the surface which correlate with those of the velocity field beneath it are advected with the mean velocity. Indeed, the planar correlation functions in figure 9(a, b) have a circular central peak. We also find that surface structures are not associated uniquely with the rotational part of the subsurface velocity field; they are equally correlated with the strain part  $\xi_S$  of  $\xi = (1/g)(\mathbf{u} \cdot \nabla)\mathbf{u}$ .

The maximum of the correlation  $C_{\xi, \nabla h}(0) = 0.5$ ; it is not equal to 1, most likely because the shed vortices are irregular and cause structures other than dimples above vortex cores – structures not captured in our measured correlations. The value of the correlation  $-C_{|\omega_z|, h}(0)$  that we find can be compared well to those found by Dabiri & Gharib (2001); Dabiri (2003;  $C_{\omega_z, h}(0) = 0.2$ ) for vortices in a vertical shear layer †; and Tsai (1998;  $C_{|\omega_z|, h}(0) = 0.5$ ) in numerical simulations of turbulence generated by a horizontal shear.

† Due to the experimental arrangement used,  $\omega_z < 0$  in their experiments.

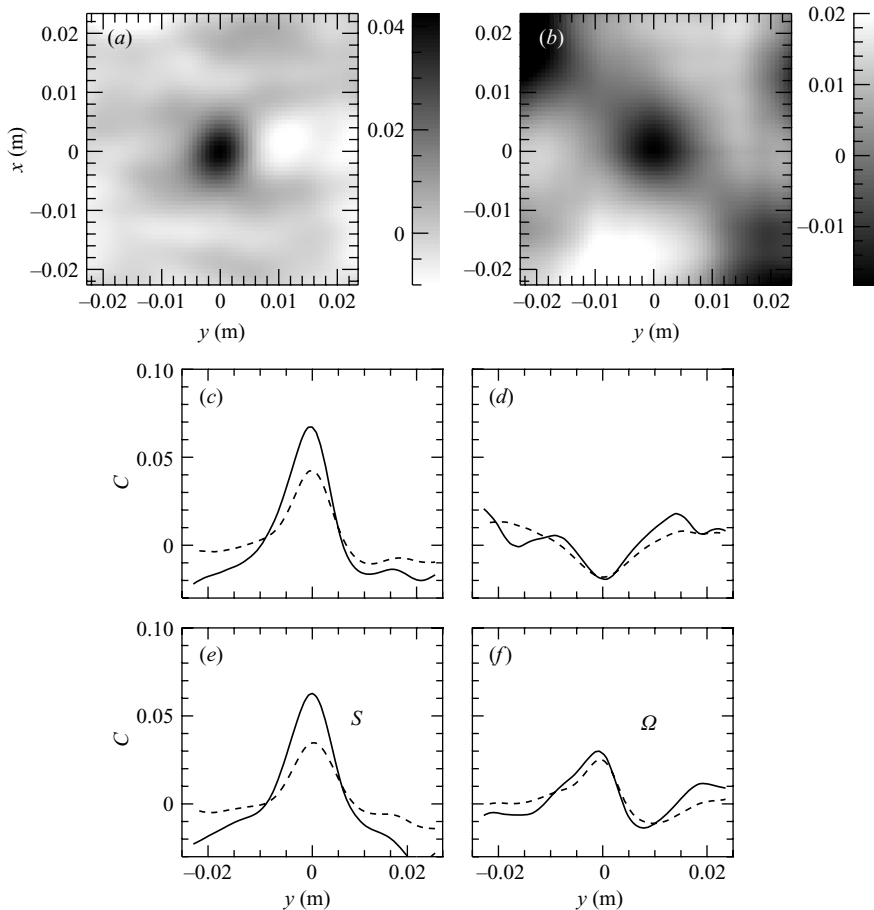


FIGURE 10. Correlations between the surface shape and the velocity field in fully developed turbulence. Planar correlation functions (a)  $C_{\xi, \nabla h}(\mathbf{r})$  and (b)  $C_{|\omega_z|, h}$ . The vertical ( $x$ ) coordinate of the surface gradient field was reconstructed using Taylor's hypothesis. (c) Full line: line correlation function  $C_{\xi, \zeta}^l(y)$ . (d) Full line: line correlation function  $C_{|\omega_z|, h}^l(y)$ . (e) Full line: line correlation function  $C_{\xi_S, \zeta}^l(y)$ . (f) Full line: line correlation function  $C_{\xi_\Omega, \zeta}^l(y)$ . The dashed lines in (c)–(f) are the corresponding planar correlation functions at  $x=0$ . The line correlations do not use Taylor's hypothesis.

### 3.2. Fully developed turbulence

Figure 10 shows the correlation functions  $C_{\xi, \zeta}$ ,  $C_{\xi_S, \zeta}$ ,  $C_{\xi_\Omega, \zeta}$  and  $C_{|\omega_z|, h}$  for fully developed turbulence generated by the active grid ( $Re_\lambda = 157$ ). As the surface is more severely wrinkled, it is now important to allow for the surface tension terms and correlate with the field  $\zeta = \nabla h - ((\sigma/\rho)\nabla)(\nabla^2 h)$  (1.3), not just with the surface gradient  $\nabla h$ . This is especially important at larger Reynolds numbers.

The maximum of the correlation functions at  $r=0$  is now 'one order of magnitude' smaller than the maximum correlations found for vortex shedding in figure 9. The planar correlations, with the  $x$ -coordinate reconstructed from time delays and using Taylor's hypothesis are shown in figure 10(a, b), while the corresponding line correlations  $C_{\xi, \zeta}^l$ ,  $C_{\xi_S, \zeta}^l$ ,  $C_{\xi_\Omega, \zeta}^l$  and  $C_{|\omega_z|, h}^l$  are shown in figure 10(c–f). The planar correlation filters structures that are convected frozen by the mean flow velocity.

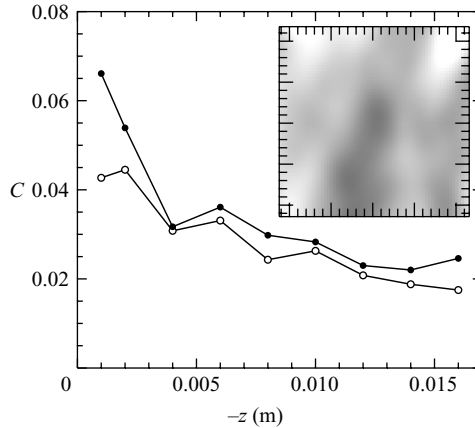


FIGURE 11. Dependence of the maximum correlations  $C_{\xi,\zeta}^l(0)$  (closed dots) and  $C_{\xi,\zeta}(0,0)$  (open circles) on the depth below the surface for turbulence generated with the active grid with  $Re_\lambda = 173$  (25OPT in table 1). Inset: correlation function at  $z = -0.016$  m, the scales are the same as those of figure 10(a).

Figure 10(a, c) illustrates that for  $C_{\xi,\zeta}$  and  $C_{\xi_s,\zeta}$  this reduces the correlation compared to the unfiltered ones,  $C_{\xi,\zeta}^l$  and  $C_{\xi_s,\zeta}^l$ . Indeed, due to the increased turbulence level, structures no longer remain frozen.

We also find that strain rather than rotation events correlate most strongly with the surface deformations. Clearly, the intuitive picture of surface dimples above vortex cores needs to be reconsidered for fully developed turbulence. That the correlations are so small is remarkable. We conclude that the surface gradient field now contains a large random component that is uncorrelated with the velocity field. We find that the maximum correlation  $C_{\xi,\zeta}^l(0)$  does not depend strongly on the Reynolds number; it ranges from  $C_{\xi,\zeta}^l(0) = 0.09$  at  $Re_\lambda = 126$  to  $C_{\xi,\zeta}^l(0) = 0.07$  at  $Re_\lambda = 157$ .

Finally, figure 11 shows the dependence of the maximum correlation  $C_{\xi,\zeta}^l(0)$  and  $C_{\xi,\zeta}(0,0)$  on the depth below the surface. Both line and planar correlations decay with increase in depth. It appears that  $C^l$  and  $C$  only differ very close to the surface. Although at the largest depth the correlation is no longer concentrated in a circular blob such as that shown in figure 10, it remains small but non-zero at  $\mathbf{x} = 0$ . From figure 11 we conclude a decay length of the correlation of approximately 0.02 m. This length scale corresponds to the width of the layer in figures 3(d, e) and 6 in which the influence of the free surface on the subsurface velocity field is felt.

#### 4. Statistical properties of the surface crispations

The conclusion of the previous section is that the correlation between surface and turbulence is greatly reduced due to random fluctuations of the surface. We will now quantify those fluctuations precisely. We will view the line scans of the surface gradient field as a space–time measurement  $\nabla h(x, t)$  or  $\nabla h(y, t)$ , depending on how the line is oriented on the surface, and no longer try to tile those lines to surfaces by invocation of Taylor’s hypothesis.

The statistical properties of the surface are quantified by space–time correlation functions and their companion wavenumber–frequency spectra. We approach the correlation function through the cross-spectral density of the surface gradient, which

for  $\nabla_x$  and the streamwise ( $\mathbf{e}_x$ ) directionscan line reads

$$\tilde{C}_{xx}(r'\mathbf{e}_x, r''\mathbf{e}_x, \omega) = \langle h_x(r'\mathbf{e}_x, \omega) h_x(r''\mathbf{e}_x, \omega) \rangle; \quad (4.1)$$

it reads similar for  $\nabla_y$  and the spanwise ( $\mathbf{e}_y$ ) direction. Homogeneity implies that the correlation function depends on  $r = r'' - r'$ , which is nearly so in our experiments (Savelsberg *et al.* 2006). The cross-spectral density can be computed quickly, after which the normalized correlation function  $C_{xx}(r\mathbf{e}_x; \tau)$  is only a Fourier transform away.

From the possible combinations of the measured component of the surface gradient and the direction of the scan line, the ‘longitudinal’ correlations are  $C_{xx}(r\mathbf{e}_x, \tau)$  and  $C_{yy}(r\mathbf{e}_y, \tau)$ , with the ‘transverse’ correlations  $C_{xx}(r\mathbf{e}_y, \tau)$  and  $C_{yy}(r\mathbf{e}_x, \tau)$ . For isotropic surface fluctuations, the longitudinal correlations are the same,  $C^L(r, \tau) = C_{\alpha\alpha}(r\mathbf{e}_\alpha; \tau)$ ,  $\alpha = x, y$ , and similarly for the transverse ones  $C^T(r, \tau) = C_{\alpha\alpha}(r\mathbf{e}_\beta; \tau)$ ,  $\alpha \neq \beta = x, y$ . In our experiments the isotropy at  $\tau \neq 0$  is trivially broken due to the mean flow velocity, and we will now consider the zero-time correlations only. Using isotropy of the surface and the fact that the field  $\nabla h$  is ‘potential’, it is possible to derive a relation between longitudinal and transverse correlation functions, with the remarkable result

$$C^L(r) = C^T(r) + r \frac{d}{dr} C^T(r). \quad (4.2)$$

A proof of (4.2) is given in the Appendix. It is interesting to compare (4.2) to the corresponding isotropy relation for the two-dimensional ‘velocity’ field,  $C^T(r) = C^L(r) + r \frac{d}{dr} C^L(r)$ . (The corresponding relation for the three-dimensional velocity field is (2.3).) The difference between the two equations, the interchange of the  $L$  and  $T$  indices, arises because the velocity field is solenoidal ( $\nabla \cdot \mathbf{u} = 0$ ), while the surface gradient field is potential ( $\nabla \times \nabla h = 0$ ).

First we will address the isotropy of the surface crispations. We recall that by a judicious choice of the active grid protocol we can control the degree of anisotropy of the subsurface turbulence. Furthermore, by either using an active or passive grid, we can control the integral scale. Table 1 lists the turbulence properties, as well as the surface slope fluctuations in the streamwise and spanwise directions. The ratio between the streamwise and spanwise fluctuations is close to unity in all cases, except for the lowest velocity.

Longitudinal and transverse correlations are shown in figure 12, both for isotropic and anisotropic turbulences. Isotropic turbulence was stirred by the passive grid and by the active grid operated with the isotropic protocol. A similar comparison of correlation functions for the subsurface velocity fields for these three cases is shown in figure 5. For the isotropic case, the longitudinal and transverse correlations are independent of the direction, while figure 12(b) illustrates that the isotropy relation (4.2) is satisfied. We also see that the surface isotropy is slightly better for turbulence from the passive grid. With anisotropic turbulence, the longitudinal correlation function of the surface depends on the direction, and also the isotropy relation (4.2) is violated. Therefore, the surface crispations inherit their (an)isotropy from the subsurface velocity field. Further, it appears that the correlation length of the surface gradient fluctuations is proportional to the correlation length of the velocity field. As a sidenote, this also shows that the surface crispations are the result of the turbulence, rather than the active grid directly affecting the surface.

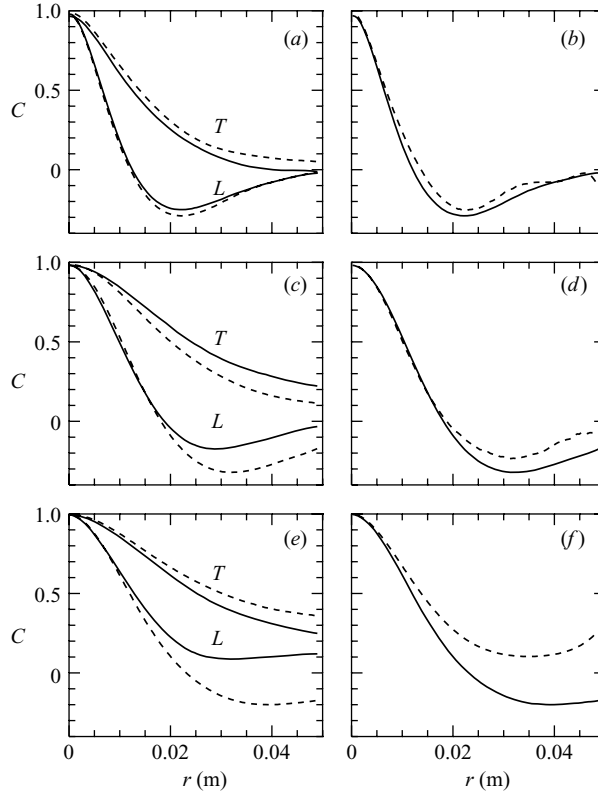


FIGURE 12. Longitudinal  $C_{\beta\beta}(r\mathbf{e}_\beta)$  ( $L$ ) and transverse  $C_{\alpha\alpha}(r\mathbf{e}_\beta)$  ( $T$ ) correlation functions of the surface gradient field. (a) Near-isotropic turbulence stirred by the passive grid (25STAT in table 1); full lines:  $\beta = x$ ; dashed lines  $\beta = y$ . (b) Full line: longitudinal  $C_{yy}(r\mathbf{e}_y)$  from (a); dashed line: longitudinal  $C^L$  computed from transverse  $C_{xx}(r\mathbf{e}_y)$  from (a), using the isotropy relation (4.2). (c) Near-isotropic turbulence stirred by the active grid (25OPT in table 1); full lines:  $\beta = x$ ; dashed lines  $\beta = y$ . (d) Full line:  $C_{yy}(r\mathbf{e}_y)$  from (c); dashed line:  $C^L$  computed from  $C_{xx}(r\mathbf{e}_y)$  from (c), using the isotropy relation (4.2). (e) Anisotropic turbulence (25RAN in table 1); full lines:  $\beta = x$ ; dashed lines  $\beta = y$ . (f) Full line:  $C_{yy}(r\mathbf{e}_y)$  from (e); dashed line:  $C^L$  computed from  $C_{xx}(r\mathbf{e}_y)$  from (e), using the isotropy relation (4.2).

While the space–time correlation functions are most sensitive to the large-scale energy-carrying structures on the surface, their wavenumber and frequency dependence is most clearly shown by the companion energy spectra:

$$E_{\alpha\alpha}(k\mathbf{e}_\beta, \omega) = \left\langle \tilde{h}_\alpha(k\mathbf{e}_\beta, \omega) \tilde{h}_\alpha^*(k\mathbf{e}_\beta, \omega) \right\rangle,$$

where  $\tilde{h}_\alpha(k\mathbf{e}_\beta; \omega)$  is the space–time Fourier transform of the gradient field  $h_\alpha(r\mathbf{e}_\beta, t)$ .

Practically, the spectrum was computed not from the cross-spectral density but from the average

$$E_{\alpha\alpha}(k\mathbf{e}_\beta, \omega) = \left\langle \left| \iint e^{i\mathbf{k}\cdot\mathbf{r} + i\omega t} h_\alpha(r\mathbf{e}_\beta, t) dr dt \right|^2 \right\rangle. \quad (4.3)$$

For the determination of  $E_{\alpha\alpha}$  the data ( $10^7$  lines, 1 h integration time) was pieced in blocks of  $4 \times 10^3$  lines (2.04 s) of 152 spatial points each. The Fourier transforms in (4.3) were done over each block, and the spectral power was averaged over 400 blocks.

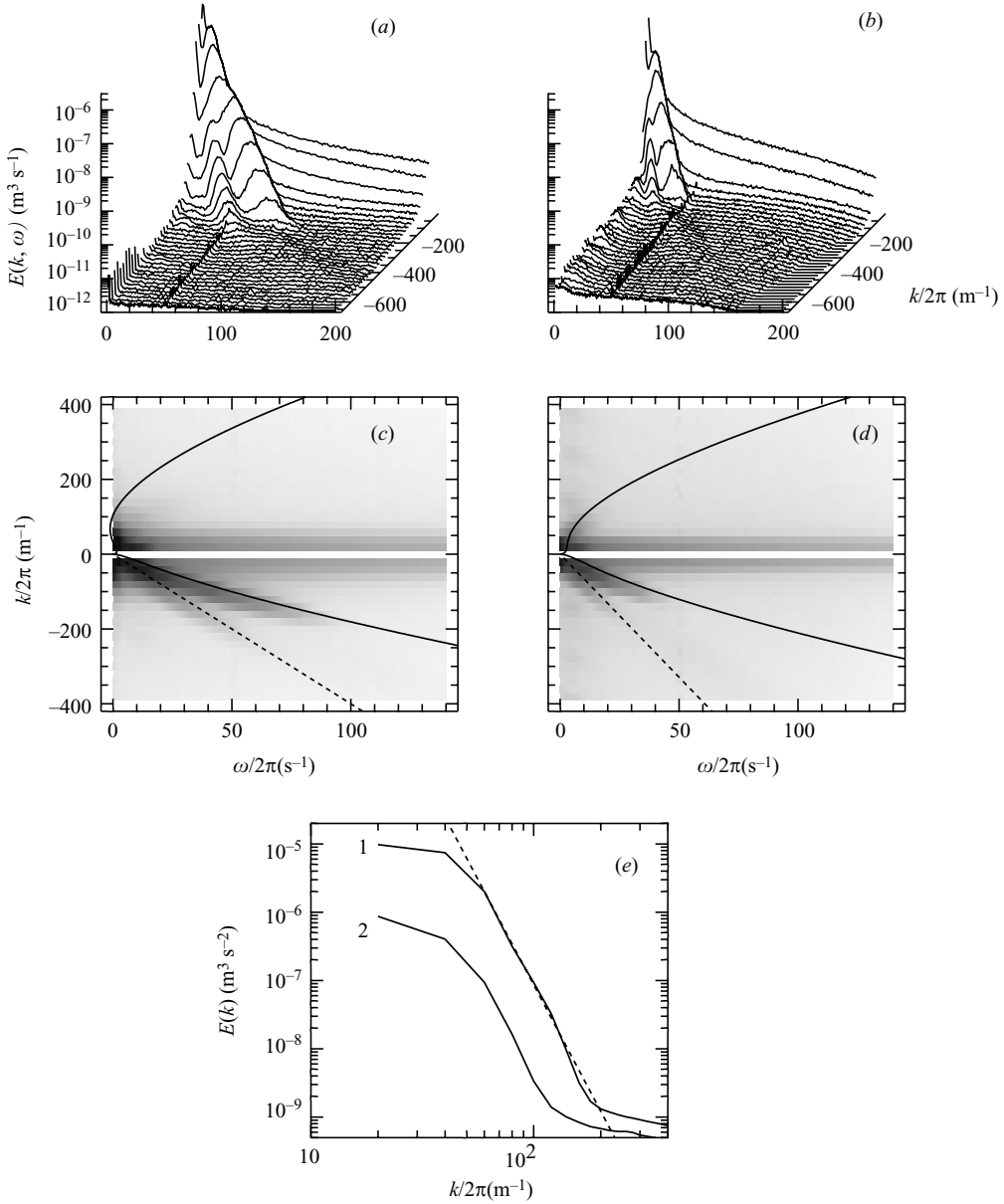


FIGURE 13. Longitudinal spectra  $E_{xx}(k\mathbf{e}_x, \omega)$  of the surface. (a), (c) Turbulence generated by the active grid with  $U = 0.25 \text{ m s}^{-1}$  and  $Re_\lambda = 172$  (25OPT in table 1). (b), (d) Active grid turbulence with  $U = 0.15 \text{ m s}^{-1}$  and  $Re_\lambda = 126$  (15OPT in table 1). (c), (d) Corresponding shading plots which also show the positive wavenumbers; the shading scale is logarithmic. Full lines: the red and blue Doppler-shifted relations for capillary-gravity waves. Dashed lines: convection by the mean flow,  $\omega = -kU$ . (e) Full line 1: wavenumber spectrum  $E_x(k) = \int_0^\infty E_x(k_x, \omega) d\omega$ , at  $Re_\lambda = 172$ ; dashed line: fit  $E_x(k) \propto k^{-6}$ ; full line 2: spectrum at  $Re_\lambda = 126$ .

While the typical length scale of the turbulent surface depends most strongly on how the turbulence is stirred, that is the integral length scale, the magnitude of the surface gradient fluctuations depends most strongly on the turbulent Reynolds number.

In figure 13 we compare  $(k, \omega)$  spectra at two Reynolds numbers. The three-dimensional plots, which for clarity are only drawn for negative wavenumbers, show

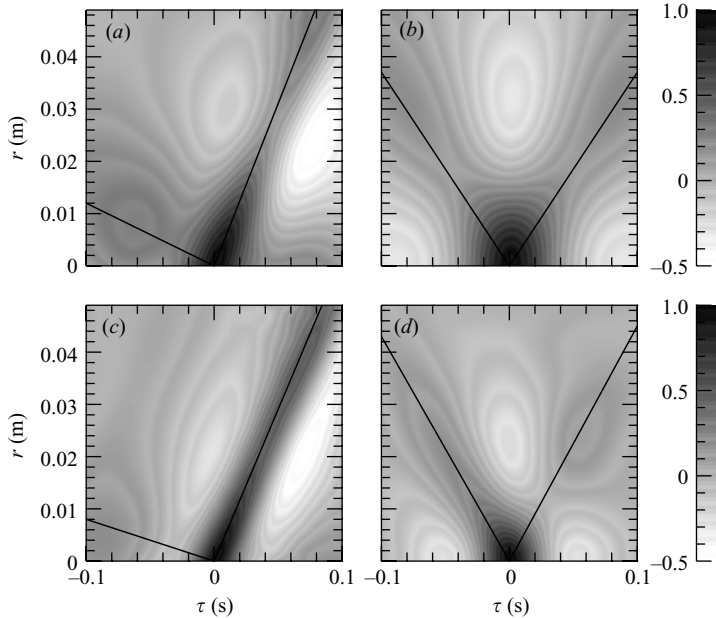


FIGURE 14. Space–time longitudinal correlation functions: (a), (c)  $C_{xx}(r\mathbf{e}_x, \tau)$  and (b), (d)  $C_{yy}(r\mathbf{e}_y, \tau)$ . (a), (b) Turbulence generated by the active grid (25OPT in table 1). (c), (d) Turbulence generated by the static grid (25STAT in table 1). Full lines indicate the convection velocity of structures: (a)  $v_f^{st} = 0.37 \text{ m s}^{-1}$ ; (b)  $v_f^{sp} = 0.37 \text{ m s}^{-1}$ ; (c)  $v_f^{st} = 0.33 \text{ m s}^{-1}$ ; (d)  $v_f^{sp} = 0.44 \text{ m s}^{-1}$ .

a ridge at  $\omega = -Uk$ , corresponding to surface structures travelling with the mean flow velocity  $U$ . These are the structures that we capture in the cross-correlations between the surface shape and the subsurface turbulence. However, they are outweighed by structures that approximately satisfy the Doppler-shifted dispersion relation of capillary–gravity waves,  $\omega = \omega_d(k) \pm Uk$ , with  $\omega_d(k) = (gk + \sigma k^3/\rho)^{1/2}$ . This is illustrated in figure 13(c, d) which also shows the positive wavenumbers. For the smallest mean velocity ( $U = 0.15 \text{ m s}^{-1}$ ) we now see the waves moving upstream.

Finally, figure 13(e) shows the corresponding wavenumber spectra  $E_x(k_x) = \int_0^\infty E_x(k_x, \omega) d\omega$ . The data suggest an algebraic behaviour  $E(k) \sim k^{-6}$ . Such a steep decay is remarkable because we measure the spectrum of the surface gradient, which is related to that of the surface elevation  $E_h(k)$  as  $E_h(k) = k^{-2} E(k)$ . This implies that the surface height spectrum is the extremely steep  $E_h(k) \sim k^{-8}$ .

It is interesting to compare the prediction of weak wave turbulence to our results. Weak wave turbulence theory (Zakharov, L’Vov & Falkovich 1992) predicts Kolmogorov-like spectra  $E(k) = C_K k^\gamma$  for weakly nonlinear surface waves, with an exponent  $\gamma$  that is determined by how waves interact and a Kolmogorov constant  $C_K$  which can be computed exactly. For pure gravity waves the exponent of the surface gradient spectrum would be  $\gamma = -1/2$ , while for capillary waves  $\gamma = -7/4$ . The crossover between the gravity and capillary regime is at  $k = (g\rho/\sigma)^{1/2}$  or  $k/2\pi \approx 60 \text{ m}^{-1}$ . Our measured exponent is much smaller than these predictions, and weak wave turbulence cannot explain the surface wave spectra.

Figure 14 shows the companion space–time correlation functions. The capillary–gravity waves show as ridges at  $U \pm v_f^{st}$  in the streamwise longitudinal correlations  $C_{xx}(r\mathbf{e}_x, \tau)$  and at  $\pm v_f^{sp}$  in the spanwise  $C_{yy}(r\mathbf{e}_y, \tau)$ . Since the wave crests are



perpendicular to the direction of propagation, these clear wave signatures are only observed in the longitudinal correlations.

The observed phase velocities,  $v_f^{sta} = 0.37 \pm 0.005 \text{ m s}^{-1}$  for the turbulence generated by the active grid and  $v_f^{sts} = 0.33 \pm 0.005 \text{ m s}^{-1}$  for the static grid, do not depend on the Reynolds number. The phase velocity  $v_f^{sta}$  corresponds to a wavelength of capillary-gravity waves  $\lambda_a = (8.4 \pm 0.2) \times 10^{-2} \text{ m s}^{-1}$ , while the velocity  $v_f^{sts}$  corresponds to  $\lambda_s = (5.2 \pm 0.2) \times 10^{-2} \text{ m s}^{-1}$ . The ratio of these wavelengths  $\lambda_a/\lambda_s = 1.6 \pm 0.1$  can be compared well to the ratio of the surface gradient length scales,  $L_{s,a} = 1.90 \times 10^{-2} \text{ m}$ ,  $L_{s,s} = 1.25 \times 10^{-2} \text{ m}$ ,  $L_{s,a}/L_{s,s} = 1.52$ , where  $L_s$  has been defined as the first zero crossing of the longitudinal correlation function  $C_{yy}(re_y)$ . In turn, this ratio of length scales can be compared to the ratio of the corresponding integral length scales of the subsurface turbulent velocity field,  $L_{l,a}/L_{l,s} = 2$ . Clearly, the surface velocities increase with increase in length scale, but probably because the manner of stirring is so different for the two cases, the surface length scale is not exactly proportional to the turbulence integral length scale. The values of the spanwise velocity  $v_f^{sp}$  are independent of the Reynolds number for the static grid,  $v_f^{sp} = 0.44 \pm 0.01 \text{ m s}^{-1}$  but decrease slightly with increase in the Reynolds number for the active grid,  $v_f^{sp} = 0.37 \text{ m s}^{-1}$  at  $Re_\lambda = 173$ , while  $v_f^{sp} = 0.44 \text{ m s}^{-1}$  at  $Re_\lambda = 126$ .

It is a remarkable feature of surface turbulence that these velocities can be determined so accurately. In §5 we will formulate a simple model that links these velocities to the size of Gaussian dimples on the surface. The emergence of the subsurface integral length scale at the surface is interesting as Komori, Nagaosa & Murakami (1990) argue that heat and mass transfer at the surface mainly occurs at this scale.

Let us now briefly return to the discussion about the applicability of Taylor's hypothesis in §2.7. If it would apply to the moving surface, the correlation functions of figure 14(a, c) would consist of a ridge at  $x = Ut$ , with the mean velocity  $U$ . Clearly, Taylor's hypothesis only applies on the mean, with the surface structures travelling at  $U \pm v_f^{st}$ .

## 5. A simple Huygens model of the turbulent surface

Our experiments show that the turbulent surface is made of capillary-gravity waves that are radiated isotropically. From the subsurface turbulent velocity field these waves inherit the integral scale, which determines their dominant wavelength and the (an)isotropy. In this section we show that the correlation functions of figure 14 can be explained by a simple model consisting of randomly distributed surface depressions with a Gaussian profile that radiate capillary-gravity waves. As (1.1) and (1.2) show, such Gaussian profiles are consistent with columnar vortices in the subsurface velocity field with a Gaussian velocity distribution.

This model will help understand the kinematics of our experiments, which are characterized by a measurement of the surface gradient along a line, while the surface is advected by the mean velocity. Therefore, the surface waves will experience a Doppler shift, depending on the relative location of their points of origin with respect to the scan line. A caveat is that in our experiments the surface shape is not correlated with vortical events only.

Let us assume sources at  $\mathbf{x}_i(t)$  which emit circular waves with spectrum  $F(k)$ . They contribute to the surface elevation at location  $\mathbf{x}$ :

$$h_i(r_i, t) = \int_0^\infty k F(k) J_0(kr_i) \cos(\omega(k)t) dk, \quad (5.1)$$

where  $\mathbf{r}_i = \mathbf{x} - \mathbf{x}_i(t)$ ,  $J_0$  the Bessel function and  $\omega(k)$  the dispersion relation of capillary-gravity waves,  $\omega(k) = gk + \sigma k^3/\rho$ . We further assume that these waves originate from surface depressions  $h_0(r)$  at  $t=0$ , with  $F(k)$ , the Fourier-Bessel transform of the initial profile,

$$F(k) = \frac{1}{4\pi} \int_0^\infty r h_0(r) J_0(kr) dr. \quad (5.2)$$

For the initial surface depression  $h_0(r)$  we assume a Gaussian profile,  $h_0(r) = \exp(-r^2/r_0^2)$ , so that

$$F(k) = \frac{1}{8\pi} r_0^2 e^{-k^2/k_0^2}, \quad (5.3)$$

with  $k_0 = 2/r_0$ . From (1.1) and (1.2) it follows that such a surface shape is consistent with a Gaussian columnar vortex with radius  $2r_0$ . At the point  $\mathbf{x}$  of observation, these waves contribute to the surface elevation  $h(\mathbf{x}, t)$ ,

$$h(\mathbf{x}, t) = \sum_i h_i(r_i, t_i), \quad (5.4)$$

where we choose for each source a random origin of time, by setting  $\cos(\omega(k)t + \phi_i)$ , with  $\phi_i$  uniformly random on  $[0, 2\pi]$ . Finally, the gradient field contributions follow from 5.1:

$$\nabla h_i(r_i, t) = -\frac{\mathbf{x}}{r_i} \int_0^\infty k^2 F(k) J_1(kr_i) \cos(\omega(k)t) dk. \quad (5.5)$$

The sources are randomly sprinkled on the simulation domain and subsequently advected by the mean flow,  $\mathbf{x}_i(t) = \mathbf{x}_{0i} + U\mathbf{e}_x t$ . The random distribution of the sources causes a random Doppler shift of the measured surface frequency. Figure 15(b) shows that far away from a single source, the wave maxima of

$$\int_0^\infty \cos(\omega(k)t - kr) e^{-k^2/k_0^2} dk \quad (5.6)$$

spread with a velocity  $v_s$  which is approximately the phase velocity of waves with the characteristic wavelength  $\lambda_0 = 2\pi/k_0 = \pi r_0$  of  $F(k)$ .

For the case of many randomly sprinkled sources figure 15(a) shows the longitudinal space-time correlation function  $C_{xx}(r\mathbf{e}_x, \tau)$  of the streamwise arrangement with  $U = 0.25 \text{ m s}^{-1}$  and all sources having  $r_0 = 0.045 \text{ m}$ . The correlation function shows both blue and red Doppler-shifted velocities,  $U \pm v_s$ , with the surface velocity  $v_s = 0.67 \text{ m s}^{-1}$ . This is larger than the experimentally observed  $v_s$ , which points to a smaller  $r_0$ .

For small  $r_0$ , figure 15 illustrates that the surface velocity of the numerical simulation approximately follows that of (5.6). It appears that for given  $\sigma, \rho, g$ , the only length-scale in the model is  $r_0$ ; variation of the average source separation by the factor 2 did not affect  $v_s$ .

Our simple kinematic model associates a surface velocity  $v_s = 0.38 \text{ m s}^{-1}$  with a length scale  $r_0 = 0.021 \text{ m}$ . This surface velocity is close to the one measured in turbulence generated by the active grid. The radius of the corresponding columnar vortices would then be  $2r_0$ . Although this is comparable to the integral scale of the subsurface velocity field ( $L = 0.08 \text{ m}$ ), we realize that a model of Gaussian vortices is too simple. Indeed, our model does not predict the occurrence of relative large frequencies in the measured  $k, \omega$  spectra. However, we believe that the model correctly represents the kinematics of the experiments. Clearly, more work is needed to relate

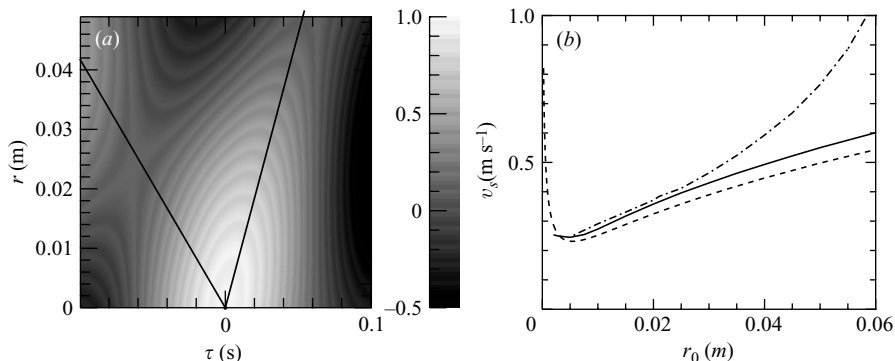


FIGURE 15. A simple model in which sources are randomly sprinkled on the surface which radiate capillary–gravity waves from Gaussian initial depressions,  $h_0(r) = -\exp(-r^2/r_0^2)$ , with  $r_0 = 0.045$  m. The entire surface moves with the mean velocity  $U = 0.25$  m s $^{-1}$ . (a) Streamwise longitudinal correlation function  $C^L(r, \tau)$  of  $\nabla_x h$ ; full lines:  $r = U \pm v_s \tau$ , with  $v_s = 0.67$  m s $^{-1}$ . (b) Surface velocity  $v_s$  as a function of the source radius  $r_0$ . Dash–dotted line: numerical simulation; full line: as predicted by (5.6); dashed line: phase velocity of capillary–gravity waves  $\omega(k)/k$  at  $\lambda = 2\pi/k = \pi r_0$ .

the spectrum of the sources  $F(k)$  to the statistics of events in the subsurface velocity field.

## 6. Conclusion

In this paper we have studied the interaction of well-defined turbulence inside a flow with the fluctuations of its free surface. As anticipated by our estimates of the Froude and Weber numbers in §1, this interaction is relatively weak if expressed in terms of the integral length scale  $L$  of the turbulence.

Now that we have measured the surface properties, we can use them to recompute the Froude and Weber numbers in terms of the characteristic surface elevation and curvature, namely  $Fr = (\langle u^2 \rangle + \langle v^2 \rangle)/2g\langle h^2 \rangle^{1/2}$  and  $We = \rho(\langle u^2 \rangle + \langle v^2 \rangle)/4\sigma\langle h_{yy}^2 \rangle^{1/2}$ , where it should be noticed that, in view of the discussion in §3, the measured surface height fluctuations  $\langle h^2 \rangle^{1/2}$  are only approximate, while in view of the limited applicability of Taylor’s hypothesis (§2.7),  $2\langle h_{yy}^2 \rangle^{1/2}$  is used to estimate  $\langle (\nabla^2 h)^2 \rangle^{1/2}$ .

For near-isotropic turbulence with the highest  $Re_\lambda$  reached in this experiment (250PT in table 1) we find that  $Fr = 0.07$  and  $We = 0.7$ , while for the case of vortex shedding in §3.1,  $Fr = 0.6$  and  $We = 3$ . These numbers suggest that in the case of fully developed turbulence, the turbulent energy mainly couples with capillary energy, while the surface above irregular vortices shed by a surface-piercing cylinder (figures 8 and 9) is dominated by gravity, as is also evidenced by the large correlation observed in figure 9.

For surface turbulence, Taylor’s hypothesis in which turbulent structures are advected with the mean velocity  $U$  approximately applies at the large scales but not at the small scales. The large-scale correlation functions of figures 9 and 10 are approximately isotropic, but  $\langle h_{xx}^2 \rangle^{1/2}$  deduced using Taylor’s hypothesis,  $\langle h_{xx}^2 \rangle^{1/2} = \langle h_{xt}^2/U^2 \rangle^{1/2}$ , is approximately three times larger than  $\langle h_{yy}^2 \rangle^{1/2}$ , although the surface is near-isotropic.

The emergence of capillary–gravity waves in our experiments is surprising because the subsurface turbulence velocity fluctuations are an order of magnitude smaller

than the minimum phase velocity of capillary-gravity waves ( $v_f \approx 0.23 \text{ m s}^{-1}$ ), and a profound question concerns the excitation mechanism of these waves. In order to understand the kinematical aspects of these waves, we have proposed a simple model in §5. Although it accounts for the velocity of the waves given the size of the subsurface structures, it is only the first step. We believe that the model should be amendable to analytic treatment. Thus, it should lead to the solution of the inverse problem: given the statistics of the surface crispations, what are the elementary excitations of the surface by the turbulence beneath it?

Clearly, the challenge for future experiments will be to create stronger turbulence, possibly with turbulent velocities that approach the minimum velocity of capillary-gravity waves. This cannot be done in the grid-generated channel flow in this paper, as reaching those velocities would require an increase in the pumping power of three orders of magnitude. An interesting variant of an active grid to create free surface turbulence with zero mean flow was recently proposed by Variano, Bodenschatz & Cowen (2004). However, a matter of concern is the homogeneity and isotropy of the generated turbulence.

This work is part of the research programme of the Stichting voor Fundamenteel Onderzoek der Materie (FOM), which is financially supported by the Nederlandse Organisatie voor Wetenschappelijk Onderzoek (NWO). We thank Ad Holten for constructing the surface scanner and GertJan van Heijst for his encouragement, and we are greatly indebted to Anders Andersen, Bernard Geurts and Carl Tipton for many helpful discussions.

### Appendix. Isotropy relation for a surface

A consequence of the fact that  $h_x$  and  $h_y$  are the gradient of scalar field  $h(x, y)$  is that they form a potential field:

$$\nabla \times (\nabla h) = \frac{\partial}{\partial x} h_y - \frac{\partial}{\partial y} h_x = 0. \quad (\text{A } 1)$$

We can use this to derive the relation between the transverse and longitudinal correlation functions for the surface slopes, via the surface slope covariance tensor, defined by

$$\mathbf{R}(\mathbf{r}) = \begin{pmatrix} R_{xx}(\mathbf{r}) & R_{xy}(\mathbf{r}) \\ R_{yx}(\mathbf{r}) & R_{yy}(\mathbf{r}) \end{pmatrix} = \begin{pmatrix} \langle h_x(\mathbf{x})h_x(\mathbf{x} + \mathbf{r}) \rangle & \langle h_x(\mathbf{x})h_y(\mathbf{x} + \mathbf{r}) \rangle \\ \langle h_y(\mathbf{x})h_x(\mathbf{x} + \mathbf{r}) \rangle & \langle h_y(\mathbf{x})h_y(\mathbf{x} + \mathbf{r}) \rangle \end{pmatrix}. \quad (\text{A } 2)$$

Using (A 1) we find that

$$\frac{\partial}{\partial r_x} R_{xy}(\mathbf{r}) - \frac{\partial}{\partial r_y} R_{xx}(\mathbf{r}) = 0, \quad (\text{A } 3)$$

and similarly

$$\frac{\partial}{\partial r_y} R_{yx}(\mathbf{r}) - \frac{\partial}{\partial r_x} R_{yy}(\mathbf{r}) = 0. \quad (\text{A } 4)$$

In any isotropic field, we can write the covariance tensor as a combination of  $r_i r_j$  and  $\delta_{ij}$ , which defines the (scalar) longitudinal covariance function  $R^L(r)$  and the transverse covariance function  $R^T(r)$  (Pope 2000)

$$R_{ij}(\mathbf{r}) = (R^L(r) - R^T(r)) \frac{r_i r_j}{r^2} + R^T(r) \delta_{ij},$$

so that

$$R_{xx}(\mathbf{r}) = (R^L(r) - R^T(r))\frac{r_x^2}{r^2} + R^T(r) \quad \text{and} \quad R_{xy}(\mathbf{r}) = (R^L(r) - R^T(r))\frac{r_x r_y}{r^2}.$$

Either (A 3) or (A 4) can now be used to find the relation between  $R^L(r)$  and  $R^T(r)$ . We start by calculating explicitly the derivatives:

$$\begin{aligned} \frac{\partial R_{xy}}{\partial r_x} &= \left( \frac{dR^L}{dr} - \frac{dR^T}{dr} \right) \frac{r_x^2 r_y}{r^3} + (R^L - R^T) \frac{r_y}{r^2} \left( 1 - \frac{2r_x^2}{r^2} \right) \\ \frac{\partial R_{xx}}{\partial r_y} &= \left( \frac{dR^L}{dr} - \frac{dR^T}{dr} \right) \frac{r_x^2 r_y}{r^3} - (R^L - R^T) \frac{2r_y r_x^2}{r^4} + \frac{dR^T}{dr} \frac{r_y}{r}. \end{aligned}$$

Substitution of these expressions in (A 3) leads to the relation between the transversal and longitudinal covariance functions,

$$R^L = R^T + r \frac{d}{dr} R^T,$$

and since the r.m.s. of the slope is independent of the direction the desired relation between the longitudinal and transverse correlation function becomes

$$C^L = C^T + r \frac{d}{dr} C^T.$$

Performing similar substitutions in (A 4) obviously leads to the same result.

#### REFERENCES

- BERNAL, L. P. & KWON, J. T. 1989 Vortex ring dynamics at a free surface. *Phys. Fluids A* **1**, 449–451.
- BORUE, V., ORSZAG, S. A. & STAROSLESKY, I. 1995 Interaction of surface waves with turbulence: direct numerical simulations of turbulent open channel flow. *J. Fluid Mech.* **286**, 1–23.
- BROCCHINI, M. & PEREGRINE, D. H. 2001a The dynamics of strong turbulence at free surfaces. Part 1. Description. *J. Fluid Mech.* **449**, 225–254.
- BROCCHINI, M. & PEREGRINE, D. H. 2001b The dynamics of strong turbulence at free surfaces. Part 2. Free-surface boundary conditions. *J. Fluid Mech.* **449**, 255–290.
- BRUMLEY, B. H. & JIRKA, G. H. 1987 Near-surface turbulence in a grid-stirred tank. *J. Fluid Mech.* **183**, 235–263.
- CALMET, I. & MAGNAUDET, J. 2003 Statistical structure of high-Reynolds-number turbulence close to the free surface of an open-channel flow. *J. Fluid Mech.* **474**, 355–378.
- COMTE-BELLOT, G. & CORRISIN, S. 1966 The use of a contraction to improve the isotropy of grid-generated turbulence. *J. Fluid Mech.* **25**, 657–682.
- CRESSMAN, J. R., DAVOUDI, J., GOLDBURG, W. I. & SCHUMACHER, J. 2004 Eulerian and lagrangian studies in surface flow turbulence. *New J. Phys.* **6**, 53, doi: 10.1088/1367-2630/6/1/053.
- DABIRI, D. 2003 On the interaction of a vertical shear layer with a free surface. *J. Fluid Mech.* **480**, 217–232.
- DABIRI, D. & GHARIB, M. 2001 Simultaneous free surface deformation and near surface velocity measurements. *Exp. Fluids* **30**, 381–390.
- FORBES, C., LEMAN, K., OLSON, D. & BROWN, O. 1993 Eddy and wave dynamics in the south Atlantic as diagnosed from geosat altimeter data. *J. Geophys. Res.* **12**, 297–314.
- GHARIB, M. & WEIGAND, A. 1996 Experimental studies of vortex disconnection and surface connection at a free surface. *J. Fluid Mech.* **321**, 59–86.
- GLEDZER, E. 1997 On the Taylor hypothesis corrections for measured energy spectra of turbulence. *Physica D* **104** (2), 163–183.
- HANDLER, R. A., SWEAN, T. F., LEIGHTON, R. I. & SWEARINGEN, J. D. 1993 Length scales and the energy balance for turbulence near a free surface. *AIAA J.* **31**, 1998–2007.
- HONG, W.-L. & WALKER, D. T. 2000 Reynolds-averaged equations for free-surface flows with application to high-Froude-number jet spreading. *J. Fluid Mech.* **417**, 183–209.

- HUNT, J. C. R. 1984 Turbulence structure and turbulent diffusion near gas-liquid interfaces. In *Gas Transfer at Water Surfaces* (ed. W. Brutsaert & G. H. Jirka), pp. 67–82. Reidel.
- HUNT, J. C. R. & GRAHAM, J. M. R. 1978 Free-stream turbulence near plane boundaries. *J. Fluid Mech.* **84**, 209–235.
- KOMORI, S., NAGAOSA, R. & MURAKAMI, Y. 1990 Mass transfer into a turbulent liquid across the zero-shear gas–liquid interface. *AIChE J.* **36**, 957–960.
- KUMAR, S., GUPTA, R. & BANERJEE, S. 1998 An experimental investigation of the characteristics of free-surface turbulence in channel flow. *Phys. Fluids* **10**, 437–456.
- LI, F.-C., KAWAGUCHI, Y., SEGAWA, T. & SUGA, K. 2005 Wave-turbulence interaction of a low-speed plane liquid wall-jet investigated by particle image velocimetry. *Phys. Fluids* **17**, 082101.
- LOEWEN, S., AHLBORN, B. & FILUK, A. B. 1986 Statistics of surface flow structures on decaying grid turbulence. *Phys. Fluids* **29**, 2388–2397.
- MAGNAUDET, J. 2003 High-Reynolds-number turbulence in a shear-free boundary layer: revisiting the Hunt–Graham theory. *J. Fluid Mech.* **484**, 167–196.
- MAKITA, H. 1991 Realization of a large scale turbulence field in a small wind tunnel. *Fluid Dyn. Res.* **8**, 53–64.
- MYDLARSKI, L. & WARHAFT, Z. 1990 On the onset of high-Reynolds-number grid-generated wind tunnel turbulence. *J. Fluid Mech.* **320**, 331–368.
- NAGAOSA, R. 1999 Direct numerical simulation of vortex structures and turbulent scalar transfer across a free surface in a fully developed turbulence. *Phys. Fluids* **11**, 1581–1595.
- NAGAOSA, R. & HANDLER, R. A. 2003 Statistical analysis of coherent vortices near a free surface in a fully developed turbulence. *Phys. Fluids* **15**, 375–394.
- PAN, Y. & BANERJEE, S. 1995 A numerical study of free-surface turbulence in channel flow. *Phys. Fluids* **7**, 1288–1290.
- PEARSON, B. R., KROGSTAD, P.-Å. & VAN DE WATER, W. 2002 Measurements of the turbulent energy dissipation rate. *Phys. Fluids* **14**, 1288–1290.
- PEROT, B. & MOIN, P. 1995 Shear-free turbulent boundary layers. Part 1. Physical insights into near-wall turbulence. *J. Fluid Mech.* **295**, 199–227.
- PHILLIPS, O. M. 1957 On the generation of waves by turbulent wind. *J. Fluid Mech.* **2**, 417–445.
- POORTE, R. E. G. 1998 On the motion of bubbles in active grid generated turbulent flows. PhD thesis, University Twente, Enschede, The Netherlands.
- POORTE, R. E. G. & BIESHEUVEL, A. 2002 Experiments on the motion of gas bubbles in turbulence generated by an active grid. *J. Fluid Mech.* **461**, 127–154.
- POPE, S. B. 2000 *Turbulent Flows*. Cambridge University Press.
- RASHIDI, M. & BANERJEE, S. 1988 Turbulence structure in open channel flows. *Phys. Fluids* **31**, 2491–2503.
- SAVELSBERG, R., HOLTEN, A. P. C. & VAN DE WATER, W. 2006 Measurement of the gradient field of a turbulent free surface. *Exp. Fluids* **41**, 629–640.
- SHEN, L., ZHANG, X., YUE, D. K. P. & TRIANTAFYLLOU, G. S. 1999 The surface layer for free-surface turbulent flows. *J. Fluid Mech.* **386**, 167–212.
- SMOLENTSEV, S. & MIRAGHAIE, R. 2005 Study of a free surface in open-channel water flows in the regime from ‘weak’ to ‘strong’ turbulence. *Intl J. Multiphase flow* **31**, 921–939.
- SONG, M., BERNAL, L. P. & TRYGGVASON, G. 1992 Head-on collision of a large vortex ring with a free surface. *Phys. Fluids A* **4**, 1457–1466.
- STAMMER, D. 1997 Global characteristics of ocean variability from regional topex/poseidon altimeter measurements. *J. Phys. Oceanogr.* **27**, 1743–1769.
- TAYLOR, G. I. 1960 On the dissipation of eddies. In *The Scientific Papers of Sir Geoffrey Ingram Taylor, Volume 2: Meteorology, Oceanography and Turbulent Flow* (ed. G. K. Batchelor). Cambridge University Press. pp. 96–101.
- TEIXEIRA, M. A. C. & BELCHER, S. E. 2000 Dissipation of shear-free turbulence near boundaries. *J. Fluid Mech.* **422**, 167–191.
- TEIXEIRA, M. A. C. & BELCHER, S. E. 2006 On the initiation of surface waves by turbulent shear flow. *Dyn. Atmos. Oceans* **41**, 1–27.
- THOMAS, N. H. & HANCOCK, P. E. 1977 Grid turbulence near a moving wall. *J. Fluid Mech.* **82**, 481–496.
- TSAI, W.-T. 1998 A numerical study of the evolution and structure of a turbulent shear layer under a free surface. *J. Fluid Mech.* **354**, 239–276.

- VARIANO, E. A., BODENSCHATZ, E. & COWEN, E. A. 2004 A random synthetic jet array driven turbulence tank. *Exp. Fluids* **37**, 613–615.
- WALKER, D. T., LEIGHTON, R. I. & GARZA-RIOS, L. O. 1996 Shear-free turbulence near a flat free surface. *J. Fluid Mech.* **320**, 19–51.
- WEIGAND, A. 1996 Simultaneous mapping of the velocity and deformation field at a free surface. *Exp. Fluids* **20**, 358–364.
- ZAKHAROV, V., L'Vov, V. & FALKOVICH, G. 1992 *Kolmogorov Spectra of Turbulence*. Springer.
- ZHANG, C., SHEN, L. & YUE, D. K. P. 1999 The mechanism of vortex connection at a free surface. *J. Fluid Mech.* **384**, 207–241.
- ZHANG, X. 1995 Capillary-gravity and capillary waves generated in a wind wave tank: observations and theories. *J. Fluid Mech.* **289**, 51–82.
- ZHANG, X. & COX, C. S. 1994 Measuring the two-dimensional structure of a wavy water surface optically: a surface gradient detector. *Exp. Fluids* **17**, 225–237.